Sailin Liu, Ruizhi Zhang, Jianfeng Mao, Jodie Yuwono, Cheng Wang, Kenneth Davey, Zaiping Guo

Design of electrolyte for boosted aqueous battery performance: A critical review and perspective

Applied Physics Reviews, 2023; 10(2):021304-1-021304-32

Applied Physics Reviews REVIEW scitation.org/journal/are

Design of electrolyte for boosted aqueous battery performance: A critical review and perspective

Cite as: Appl. Phys. Rev. **10**, 021304 (2023); doi: 10.1063/5.0140107
Submitted: 27 December 2022 · Accepted: 13 March 2023 ·
Published Online: 24 April 2023

Sailin Liu,[1] Ruizhi Zhang,[1,2,3] Jianfeng Mao,[1] Jodie Yuwono,[1] Cheng Wang,[1] Kenneth Davey,[1] and Zaiping Guo[1,a)]

AFFILIATIONS

[1]School of Chemical Engineering & Advanced Materials, Faculty of Sciences, Engineering & Technology, The University of Adelaide, Adelaide 5005, Australia
[2]The Institute for Superconducting and Electronic Materials, the Australian Institute for Innovative Materials, University of Wollongong, Wollongong, New South Wales 2500, Australia
[3]Advanced Technology Institute, Department of Electrical and Electronic Engineering, University of Surrey, Guildford, Surrey GU2 7XH, United Kingdom

Note: This paper is part of the special collection on Energy Storage and Conversion.
[a)]**Author to whom correspondence should be addressed:** zaiping.guo@adelaide.edu.au

ABSTRACT

Aqueous alkali and multivalent metal-ion batteries are practically advantageous for large-scale energy storage because of intrinsic safety and environmental friendliness. Drawbacks, however, include low energy density and short life because of limited electrochemical stability windows (ESWs) of aqueous electrolytes and rapid degradation of electrode materials with high water activity. Despite significant research, including water-in-salt and electrolyte additive(s), directed to the electrolyte to extend ESWs and to boost electrode stability, the practical application remains limited because of the present high cost and generally unsatisfactory performance. Although alkali and multivalent metal ions can have different coordinating structures with solvents and anions, electrolyte design strategies share fundamental mechanisms in either extending ESWs or achieving a passivation layer on the electrode material(s). Future development of aqueous batteries, therefore, is dependent on a systematic understanding and analysis of electrolyte research. Here, we report for the first time a systematic review of the design and engineering of emerging water-based electrolytes for boosted aqueous rechargeable batteries (ARBs) performance. We present a comparative summary of electrochemical stability windows and electrode/electrolyte interphases for five (5) electrolyte types; appraise strategies and the resulting impact of electrolyte properties on electrode interfacial stability; analyze *in situ* generated electrode/electrolyte interphases; classify advantages and drawbacks of selected strategies; and provide a perspective on future developments in aqueous alkali and multivalent metal-ion batteries, together with methods for the study of both electrolyte and derived interphase(s). We conclude that (1) the design of electrolytes of high concentration and hybrid and eutectic solvents are practically promising for high energy density ARBs; (2) there is a need to improve design for longer cycling life of ARBs; (3) research addresses boosting ESW of the electrolyte; and (4) it increased the understanding of the electrode/electrolyte interface stability via new electrode/electrolyte interphase structures. This review will be of benefit in the practical design of electrolyte(s) for aqueous batteries for high performance and, therefore, of interest to researchers and manufacturers.

TABLE OF CONTENTS

I. INTRODUCTION

The sustainable uptake of renewable energy and rapid development in smart grids requires large-scale electrical-energy-storage (EES) to buffer intermittent generation from solar and wind. Because global grid-scale battery storage is experiencing significant demand, an EES system is, therefore, necessary to economically provide rapid, efficient, and high-energy-density storage, together with operation in harsh conditions. Among various EES systems, the aqueous rechargeable M-ion (M = Li, Na, K, Zn, Mg, and Ca) battery appears practically promising because of high safety, low toxicity, high ionic conductivity, and high theoretical capacity.[1–3]

Over the past decade, there has been a highly significant increase in the number of publications reporting aqueous rechargeable batteries (ARBs), as displayed in Fig. S1. However, the narrow theoretical electrochemical stability window (ESW) for water of 1.2 V results in hydrogen and oxygen evolution reactions (HER and OER, respectively) and restricts selection for active electrode materials. Extending ESW is a long-standing practical difficulty in developing ARBs. In 2015, this was addressed via introducing a highly concentrated electrolyte [21 m lithium bis(trifluoromethane sulphonyl)imide (LiTFSI)] in aqueous Li-ion batteries (ALIBs) that suppressed unwanted electrolysis of water, together with expanding the voltage window to 3.0 V with formation of a solid–electrolyte interphase (SEI).[4,5] Following this, selected effort, including using a high concentration of binary salt(s), has been made to extend ESW for electrolytes in ARBs. Importantly, a continuous enlargement in ESWs through targeted electrolyte design modulation offers increased choice in electrode materials to boost energy density and cycling life of ARBs.

Among various ARBs, rechargeable aqueous alkali ion batteries are developed more extensively because of comprehensive research on non-aqueous Li-ion batteries. Led by ALIBs, significant progress on design for liquid electrolytes has been made through high concentration, hybrid organic/water solvents, deep eutectic solvents (DES), and hybrid ionic liquids (ILs)/water-in-salt (WIS). Xu *et al.*[6] reported a deep eutectic electrolyte with urea to boost ESW for ALIBs from 2.0 to 3.3 V, with a highly significant energy density of 103 W h kg^{-1} that is meaningfully greater than for "best" NiMH technology of 100 W h kg^{-1}.[7] Although the theoretical specific capacity and electrochemical potential for metallic Na and K are inferior to those for Li, an abundance and low-cost are practically attractive. Significant research effort has been made on aqueous sodium ion batteries (ASIBs) and aqueous potassium ion batteries (APIBs) using this WIS strategy. For example, a 26 m sodium trifluoroacetate (NaTFA) electrolyte exhibited a high ionic conductivity of 23 mS cm^{-1} and wide ESW of 3.1 V.[8] For APIBs, a recent study on binary salts electrolyte of 61.7 m of $KN(SO_2F)_2$ (KFSI) and KSO_3CF_3 (KOTf) reported good ionic conductivity of 12 mS cm^{-1} at 30 °C and wide ESW of 2.7 V.[9]

Aqueous divalent metal-ion batteries, represented by a Zn metal anode in aqueous zinc metal batteries (AZMBs), in principle, can deliver high energy density because of a low potential of −0.762 V vs the standard hydrogen electrode and high capacity of 820 mAh g^{-1} for Zn anode. Practical difficulties remain, however, including inferior performance of positive electrode materials to dendrites formation and side reactions involving H^+ or OH^- species on the Zn metal anode. Performance of AZMBs can be boosted significantly via electrolyte design engineering for prolonged cycling of the Zn metal anode and improved stability of cathode materials.[10] There are reported studies on electrolyte additives, including $Zn(H_2PO_4)_2$[11] to construct Zn^{2+} ion conductive SEI on the Zn metal anode that inhibit HER and dendrite formation. For aqueous magnesium ion battery (AMIB), the lack of suitable electrolytes restricts development because of a desolvation "penalty" at electrode–electrolyte interface and strong electrostatic interaction with the host material that gives rise to insufficient ionic conductivity and solid-state diffusion.[12] Progress, however, has been made through a hydrated eutectic electrolyte via suppressing water activity and facilitating Mg^{2+} transport to enable a stable and high-rate organic molecule anode and copper hexacyanoferrate (CuHCF) cathode.[13] Development of aqueous calcium ion batteries (ACIBs) is supported by low polarization strength similar to that for Li^+ that avoids kinetic difficulties caused by other multivalent ions, e.g., Mg^{2+} and Zn^{2+} with high polarization strength. Although the WIS strategy provides a pathway to widen ESW and improve Ca-ion desolvation kinetics via boosted anion–cation interactions and decreased water activity,[14] the lack of storage materials and suitable electrolytes with high ionic conductivity and facile Ca^{2+} desolvation limits practical application to ACIBs.

These electrolyte strategies bring benefits, such as the ability for generating SEI and anti-freezing property, except for electrochemical performance of ARBs. These, however, are practically difficult with conventional aqueous electrolytes. ARBs enabled by advanced electrolyte strategies have practical potential to be integral components in future electricity supply systems in which significant reductions in cost might be achieved together with safe and reliable operation.

Electrolyte strategies to address the drawbacks of narrow ESW and inferior cycling life of aqueous batteries are relatively diffuse, however. Development is dependent on a clear analysis and understanding of reported research. Here, for the first time, we report, therefore, a systematic review of design and engineering of emerging water-based electrolytes for boosted ARBs performance. We present a comparative summary of ESWs and electrode/electrolyte interphases for five (5) electrolyte types and appraise strategies and resulting impact of electrolyte properties on electrode interfacial stability. We analyze *in situ* generated electrode/electrolyte interphases and classify advantages and drawbacks of selected strategies and provide a perspective on future developments, together with methods for study of both electrolyte and

derived interphase(s). We focus on rechargeable energy storage technologies, ALIBs, ASIBs, APIBs, AZMBs, AMIBs, and ACIBs. We conclude that (1) design of electrolytes of high concentration and hybrid and eutectic, solvent, are practically promising for high energy density ARBs, (2) there is a need to improve design for longer cycling life of ARBs, and research is needed to address (3) boosting ESW of the electrolyte, and (4) increased understanding of the electrode/electrolyte interface stability via new cathode electrolyte interphase (CEI) and anode SEI structures. Findings will be of benefit in practical design of electrolyte(s) for aqueous batteries for high performance and to researchers and manufacturers.

II. AQUEOUS LITHIUM-ION BATTERIES

A. Electrochemical stability windows and electrode/electrolyte interphases

In ALIBs, $LiMn_2O_4$ (LMO) is a typical cathode material because of high working voltage of 3.1–4.6 V, low-cost, and non-toxicity, while $Li_4Ti_5O_{12}$ (LTO) is an ideal anode material because of high structural stability and an appropriate insertion/de-insertion potential of ~1.55 V. An ideal working window for LMO//LTO full batteries is 1.4–4.6 V vs Li/Li^+, requiring the electrolyte to provide a wider ESW. The traditional salt-in-water electrolyte, e.g., 1 m LiTFSI, however, exhibits a narrow ESW of 2.0 V[5,15] (2.5–4.5 V vs Li/Li^+) that is insufficient to achieve the LMO//LTO full batteries. Strategies, including high concentration, hybrid solvents, eutectic solvents, and ionic liquid–WIS hybrid, can significantly widen ESW as illustrated in Fig. 1. Regarding the goal for building LMO/LTO full battery, strategy of the hybrid solvents and eutectic solvents is highly promising, as they can notably push the anodic limit to 5.0 V and cathodic limit down to 1.0 V, offering great opportunities for stable LMO//LTO batteries as well as a wide active materials choice.

Passivation of the positive and negative electrode surface through formation of the interphase between electrolyte and electrode influences the battery operational voltage range and cycling life. An effective electrolyte derived interphase not only kinetically stabilizes electrolytes at potentials far beyond their thermodynamic stability limits but also enhances the electrode stability. Particularly, an ideal electrode/electrolyte interphase should have the following characteristics: (1) good ionic conductivity and electronic insulation; (2) good thermal and chemical stabilities for reducing decomposition reactions; (3) being uniform and robust structure/composition that can block the direct contact between the electrolyte and the electrode for preventing the further decomposition of the electrolyte; and (4) good mechanical property that can cope with deformation under stress.[16] The development of electrode/electrolyte interphases under for four (4) main categories for ALIBs from these strategies is summarized in Fig. 2 and in Table I. Significant reported progress on interphases has been made via high concentration, hybrid organic/water solvents, eutectic solvents, and ionic liquid–WIS hybrid methods, where a comprehensive study was made on both cathode and anode electrolyte interphases. The success on constructing the electrode/electrolyte interphases in ALIBs with these electrolyte strategies shows potential for widening the battery operational windows and enhancing electrode stability. For example, an ether in water electrolyte [tetraethylene glycol dimethyl ether (TEGDME) in a concentrated aqueous electrolyte][17] can broaden ESW to 4.2 V (0.6–4.8 V vs Li/Li^+) and can exhibit a high stable capacity of 155.1 mAh g^{-1} at 3 C in a LMO//LTO battery. The CEI is composed of $CH_3OCH_2CH_2OLi$, $HOCH_2CH_2OLi$, $LiOCH_2CH_2OLi$, and RCH_2OLi on LMO, and the anode SEI is LiF on LTO. Obtaining CEI and SEI from differing electrolytes to broaden ESW and boost battery cycling life highlights the necessity of constructing *in situ* electrode/electrolyte interphases and stabilizing electrode performance.

B. Current developments with four (4) electrolyte types

The intercalation potential for selected electrode materials with potential relative to HER and OER is presented in Fig. 3(a). This evidences the importance of electrolyte pH on shifting HER and OER, together with a cathode/anode couple.[31] Practically, promising high voltage electrodes (>4.0 V vs Li^+/Li), including $LiMn_2O_4$, $LiCoO_2$, and $LiNiO_2$, can be coupled with low voltage electrodes for high energy output; however, this is limited by HER under an acidic

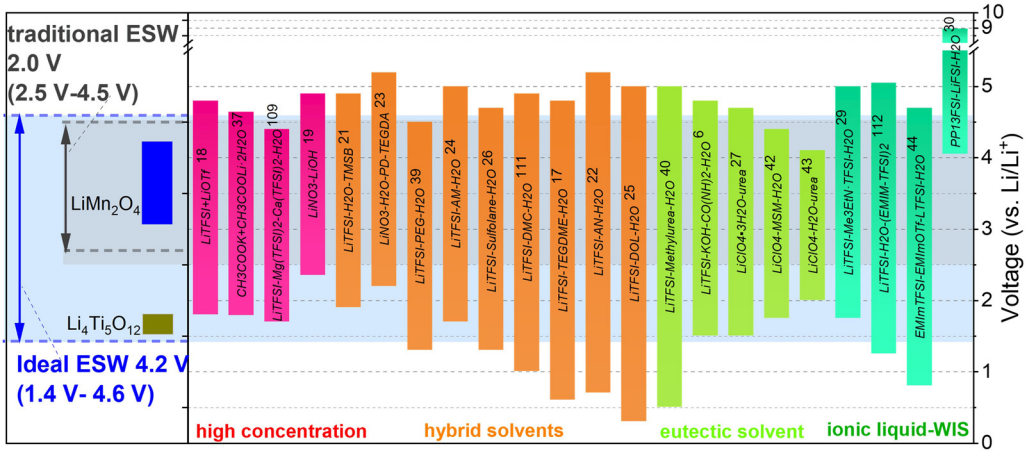

FIG. 1. Summary of ESWs of reported electrolytes under the four categories (high concentration, hybrid solvents, eutectic solvent, and ionic liquid–WIS) and charge/discharge working voltages of LMO (3.1–4.6 V) and LTO (~1.55 V) for ALIBs. The traditional ESW (2.5–4.5 V) refers to a dilute aqueous electrolyte (e.g., 1 m LiTFSI in H_2O) without any modifications. An ideal ESW (1.4–4.6 V) is defined as a safe operational voltage range of LMO//LTO full battery.

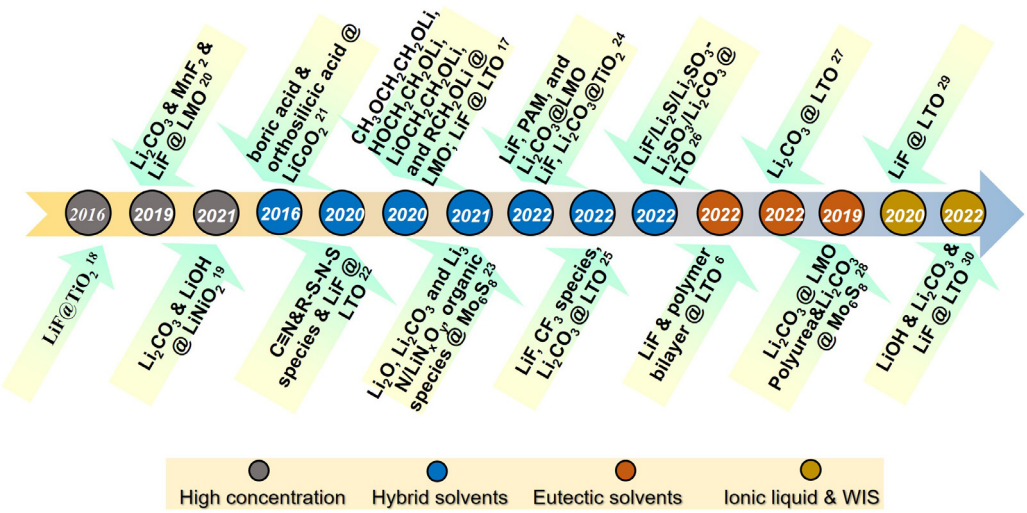

FIG. 2. Main progress in electrode/electrolyte interphases for four (4) main categories of electrolytes (high concentration, hybrid solvents, eutectic solvents, and ionic liquid–WIS) for ALIBs.[6,17–30]

electrolyte. Promoting formation of protective interphase layer is important for lowering down the cathodic limit of the electrolyte, which is closely related to the electrolyte components decomposition.

WIS is an effective way to extend the ESW toward lower cathodic limit and promotes formation of protective interphase layer on the electrode surface via salt anion reduction, which suppresses parasitic reaction of water. Computing simulations can be used to predict decomposition of electrolyte components during charging discharging process. In particular, density functional theory (DFT) prediction for reduction potential for LiOTf contact ion pair complexes in aqueous electrolyte, as shown in Fig. 3(b), gives insight into how SEI, such as LiF, is formed because of reduction of LiOTf complexes. Reduction potential for Li_2OTf and $Li_4(OTf)_2$ complexes are greater than the HER potential for H_2O and contribute to formation of the protective layer, which can suppress hydrogen evolution. Investigation using molecular dynamics (MD) gives a better description of the electrolyte system than does DFT, because coordination between each component, namely, cation, anion, and solvent, can be accurately determined. By using water-in-bi-salt (WIBS) strategy via the addition of OTf^-, the solvation structure was changed by displacement of an average of 0.5 water molecules from Li^+ solvation shells [Fig. 3(b)]. MD analysis evidences the decrease in free water molecule fraction in WIBS compared with that in WIS, resulting in an increase in ESW in this concentrated electrolyte.[18]

The long-range ordering of a particular system is practically useful for determining the solvation structures of solutes and could be studied with MD. As shown in Fig. 3(c), the coordination between each component in the electrolyte using domain analysis gives a better understanding of the solvation structure. Different anions exhibit no significant effect on interactions between Li^+ and anion in domain analysis, except that the charge-transfer will not be evenly distributed following interaction with asymmetric anions. This creates selective interaction between water molecules and anion that is reflected in the observation of high viscosity in the laboratory. However, in relation to ionic conductivity the symmetric, e.g., FSI, TFSI, and BETI, and asymmetric, e.g., TF, TFSAM, TSAC, and NF, structure and size of anions are critical [Fig. 3(d)]. FSI and TF are small anions with significant best ionic conductivities among the other anions. Specially, FSI, as a symmetric anion, has better conductivity compared with TF. Critical information for physical properties for salt anion determined from MD simulation is practically useful for design of electrolyte systems.[32]

1. Water-in-salt

Concentrated electrolyte strategy is based on high concentration of salt, typically higher than 1.0 m (mol $kg^{-1}_{solvent}$, which reduces electrochemical activity of water molecules in a Li^+ solvation sheath. As a high concentration strategy, the WIS electrolyte is defined as salt outnumbering water solvent in both weight and volume. In the WIS electrolyte, the average number of water molecules available to solvate each Li^+ is less than the "solvation numbers" required to establish a normal Li^+ solvation sheath for dilute concentration. As a result, both the Li^+ solvation sheath structure and the bulk electrolyte liquid structure are significantly changed compared with the low concentration electrolyte, resulting in widened ESW, together with an altered interfacial chemistry for cathode and anode. A benefit from the extended ESW with 21 m LiTFSI electrolyte, which exhibits a cathodic limit potential of 1.9 V (vs Li/Li^+) [Fig. 4(a)], is that the TiS_2 anode with a low redox potential allows Li^+ intercalation before HER.[33] To inhibit further the reduction activity of water and improve SEI composition, Suo *et al.*[18] reported a WIBS strategy via using a 21 m LiTFSI and 7 m LiOTf mixed electrolyte. This WIBS electrolyte exhibited a significantly increased cathodic limit of 1.83 V, allowing a reversible lithiation/de-lithiation of TiO_2 within the ESW. The average output voltage of 2.1 V exhibited by $LiMn_2O_4//TiO_2$ full battery in this WIBS electrolyte is significantly greater than that for $LiMn_2O_4//LiTiPO_4$ and $LiMn_2O_4//Mo_6S_8$ as compared in Fig. 4(b). Additionally, the cycling performance for the full battery is significantly boosted because of the optimized LiF-dominated SEI from reduction of LiTFSI and LiOTf.

TABLE I. Aqueous alkali metal ion batteries. (The symbol "∗" represents there is no data available from the referred work.).

Battery		Electrolyte property: Electrolyte	ESW	Ionic conductivity (mS cm^{-1})	Full battery: Cathode	Anode	Capacity (mAh g^{-1})	Current rate	Cycling number	Interphase(s): CEI	SEI	Ref.
Alkali metal ion vs Li/Li^+	High concentration	21 m LiTFSI + 7 m LiOTf/H_2O	1.8–4.9	6.5	$LiMn_2O_4$	Carbon-coated TiO_2	48	75 mA g^{-1}	100	∗	LiF	18
		21 m LiTFSI/H_2O	1.8–4.8	∗	$LiMn_2O_4$	TiS_2	58	240 mA g^{-1}	50	∗	∗	33
		21 m LiTFSI + 7 m LiOTf/H_2O	∗	∗	$LiVPO_4F$	Pre-coating 0.5 M LiTFSI-HFE + 10 wt. % polyethylene oxide gel graphite	125	0.3 C	50	∗	LiF and organic C–F species	34
		21 m LiTFSI + 7 m LiOTf/H_2O	1.8–4.9	∗	$LiMn_2O_4$	Sulfur-Ketjen black	335	0.2 C	1000	∗	LiF	36
		$LiNO_3$:H_2O (1:2.5)	2.35–4.9	∗	∗	∗	∗	∗	∗	∗	∗	35
		40.4 m KAc + 9.8 m LiAc·$2H_2O$	1.79–4.64	8	$LiMn_2O_4$	AC	30	2000	3000	∗	K_2CO_3	37
		21 m LiTFSI + 7 m LiOTf/H_2O	∗	∗	$(LiBr)_{0.5}(LiCl)_{0.5}$–graphite	Graphite	125	44	150	∗	∗	107
		9.5 m $LiNO_3$ + LiOH (pH = 10)/H_2O	∗	∗	$LiNiO_2$	∗	150	∗	50	Li_2CO_3, LiOH	∗	19
		1:4 LiTFSI:H_2O	∗	∗	$VOPO_4$ nH_2O	Active carbon	118	1 A g^{-1}	200	∗	∗	108
		21 m LiTFSI + $Mg(TFSI)_2$ + $Ca(TFSI)_2$/H_2O	1.7–4.4	8.8 (Mg) and 6.2 (Ca)	$LiCoO_2$	$Li_4Ti_5O_{12}$	132.4	175	50	∗	LiF	109
		21 m LiTFSI + 7 m LiOTf/H_2O	∗	∗	$K_3[Fe(CN)_6]$	Carbon-coated anatase TiO_2	100	∗	60	∗	Li_2CO_3, LiF, and Li_2O	110
		21 m LiTFSI/7 m LiOTf/H_2O	∗	∗	$LiMn_2O_4$	$K_3[Fe(CN)_6]$	∗	∗	∗	Li_2CO_3, MnF_2 and LiF	∗	20
	Hybrid solvents	21 m LiTFSI/H_2O + 0.1 wt. % tris(trimethylsilyl) borate (TMSB)	1.9–4.9 V	∗	$LiCoO_2$	Mo_6S_8	40	2.5 C	1000	Boric acid and orthosilicic acid	∗	21
		15.3 m LiTFSI/AN + H_2O	0.7–5.2	2.99	$LiMn_2O_4$	$Li_4Ti_5O_{12}$	160	1 C	300	∗	Nitrile (CN), sulfamide (R–S–N–S) species, and LiF	22
		15 m LiTFSI/TEGDME + H_2O	0.6–4.8	0.63	$LiMn_2O_4$	$Li_4Ti_5O_{12}$	155.1	3 C	300	$CH_3OCH_2CH_2OLi$, $HOCH_2CH_2OLi$, $LiOCH_2CH_2OLi$, and RCH_2OLi	LiF	17
		30.25 m LiTFSI/DMC + H_2O	1–4.9	∗	$LiNi_{0.5}Mn_{1.5}O_4$	$Li_4Ti_5O_{12}$	40	50	50	∗	∗	111

TABLE I. (*Continued.*)

Battery		Electrolyte property: Electrolyte	ESW	Ionic conductivity (mS cm^{-1})	Full battery: Cathode	Anode	Capacity (mAh g^{-1})	Current rate	Cycling number	Interphase(s): CEI	SEI	Ref.
		2 m LiTFSI/ 94%PEG + 6%H_2O	1.3–4.5	0.8	$LiMn_2O_4$	$Li_4Ti_5O_{12}$	40	1 C	300	*	*	39
		12.5 m $LiNO_3$/ H_2O + PD + TEGDA	2.2–5.2	19.9	$LiMn_2O_4$	Mo_6S_8	100	1 C	250	*	Li_2O, Li_2CO_3, Li_3N/LiN_xO_y, and organic species	23
		21 m LiTFSI acrylamide (AM) + H_2O	1.7–5.0	9.6	$LiMn_2O_4$	L-TiO_2	157	1 C	200	LiF, PAM, Li_2CO_3	LiF, Li_2CO_3	24
		10 m LiTFSI/DOL + H_2O	0.3–5.0	1.0	$LiMn_2O_4$	$Li_4Ti_5O_{12}$	100	0.5 C	100	*	LiF, CF three species, Li_2CO_3	25
		1 M LiTFSI/ sulpholane + H_2O (molar ratio 8:8)40	1.3–4.7	2.5	$LiMn_2O_4$	$LiAlO_2$ coated on $Li_4Ti_5O_{12}$	54	5 C	1000	*	LiF/Li_2S/ Li_2SO_3-Li_2SO_3/Li_2CO_3	26
	Deep eutectic solvents	1.8:1:1 MSM–$LiClO_4$–H_2O	1.75–4.4	1.41	$LiMn_2O_4$	$Li_4Ti_5O_{12}$	40	4.5 C	1000	*	*	42
		4.5 m LiTFSI/KOH + urea + H_2O	1.5–4.8	1	$Li_{1.5}Mn_2O_4$	$Li_4Ti_5O_{12}$	60	1.5 mA h cm^{-2}	1000	*	LiF + polymer bilayer	6
		5 M $LiClO_4$ $3H_2O$/urea	1.5–4.7	26	$Li_{1.5}Mn_2O_4$	$Li_4Ti_5O_{12}$	60	10 C	1000	*	Li_2CO_3	27
		1:3:2 $LiClO_4$–H_2O–urea	2.0–4.1	*	$LiMn_2O_4$	Mo_6S_8	30	10 C	2000	Li_2CO_3	Polyurea abd Li_2CO_3	43
		LiTFSI/methylurea + H_2O	0.5–5.0		$LiMn_2O_4$	NbO_2	*	*	*	*	*	40
	IL and WIS hybrid	42 m LiTFSI + 21 m Me3EtN·TFSI/H_2O	1.75–5.0	0.91	$LiMn_2O_4$	$Li_4Ti_5O_{12}$	60	0.2 C	150	*	LiF	29
		$PP_{13}FSI$ + 35 m LiFSI/ H_2O	4.05–8.95	3	$LiMn_2O_4$	$Li_4Ti_5O_{12}$	150	2 C	1000	*	LiOH, Li_2CO_3, and LiF	30
		EMImTFSI and EMImOTf + 40 m LTFSI/H_2O	0.8–4.7	1.2	$LiNi_{0.8}Mn_{0.1}Co_{0.1}O_2$	$Li_4Ti_5O_{12}$	60	1 C	300	*	*	44
		LiTFSI/$(H_2O)_{2.6}$ and LiTFSI/$(EMIMTFSI)_{2.0}$ / H_2O	1.25–5.05	3.7	Nb_2O_5	AC	100	1 A g^{-1}	3000	*	*	112
Alkali metal ion vs Na/Na^+	High concentration	1 M Na_2SO_4/H_2O	*	*	$Na_{0.44}MnO_2$	$NaTi_2(PO_4)_3$	*	*	*	*	$Ti(SO_4)_2$, H_2TiO_3	113
		37 m NaFSI/H_2O	1.78–3.48	8	$Na_3(VOPO_4)_2F$	$NaTi_2(PO_4)_3$	*	*	*	*	*	50
		17 m $NaClO_4/H_2O$	1.69–4.47	*	$Na_2MnFe(CN)_6$	$NaTi_2(PO_4)_3$	100	5 mA cm^{-2}	100	*	*	114
		9.26 M NaOTf/H_2O	1.7–4.2	*	$Na_{0.66}[Mn_{0.66}Ti_{0.34}]O_2$	$NaTi_2(PO_4)_3$	20	133 mA h g^{-1}	1500	*	NaF	47
		34 m KAc + 8 M NaAc/ H_2O	0.93–5.5	12	$Na_2MnFe(CN)_6$	$NaTi_2(PO_4)_3$/ C	32	200 mA g^{-1}	100	*	*	49
		9.0 M $NaClO_4/H_2O$	2.0–4.33	115	*	*	*	*	*	*	*	115
		9.2 m NaOTf/H_2O	*	50	$Na_2VTi(PO_4)_3$/C	$Na_2VTi(PO_4)_3$/ C	24.8	1.2 A g^{-1}	1000	*	*	51

Appl. Phys. Rev. **10**, 021304 (2023); doi: 10.1063/5.0140107

TABLE I. (*Continued.*)

Battery		Electrolyte property			Full battery					Interphase(s)		
		Electrolyte	ESW	Ionic conductivity (mS cm^{-1})	Cathode	Anode	Capacity (mAh g^{-1})	Current rate	Cycling number	CEI	SEI	Ref.
		17 m $NaClO_4/H_2O$	1.7–4.4	108	$Na_4Fe_3(PO_4)_2(P_2O_7)$	$NaTi_2(PO_4)_3$	80	1 C	200	*	Na_2CO_3 and NaOH	52
		25 m NaFSI + 10 m NaFTFSI/H_2O	1.73–4.73	*	$Na_3(VOPO_4)_2F$	$NaTi_2(PO_4)_3$	110	1 C	500	*	*	116
		17 m $NaClO_4/H_2O$	2.03–4.53	120	*	$NaTi_2(PO_4)_3$	*	*	*	*	*	117
		19 m $NaClO_4$ + 2 m NaOTf/H_2O	1.6–4.4	95.25	$Na_3V_2(PO_4)_3$	$Na_3V_2(PO_4)_3$	40	1 C	100	*	NaF, NaO, and NaOH	48
		26 m NaTFA/H_2O	1.48–4.58	23	$Na_2VTi(PO_4)_3$	$Na_2VTi(PO_4)_3$	30	2 mA cm^{-2}	300	*	CF_3, CO_3, C–C, and NaF	8
		$Na(PTFSI)_{0.65}(TFSI)_{0.14}(OTf)_{0.21}$ $3H_2O$	2.1–4.6	14	$Na_3V_2(PO_4)_2F_3$	$NaTi_2(PO_4)_3$	60	*	500	*	*	118
		18 m mixed NaPTFSI/NaTFSI/NaOTf/H_2O	2.68–3.73	*	$Na_2Mn[Fe(CN)_6]$	$NaTi_2(PO_4)_3$	120	140 mA g^{-1}	250	*	*	119
		35 m $Na(FSI)_{0.71}(FTFSI)_{0.29}/H_2O$	*	*	$Na_3(VOPO_4)_2F$	$NaTi_2(PO_4)_3$	85	130 mA g^{-1}	250	*	*	119
	Hybrid solvents	$HClO_4$ + $NaClO_4/H_2O$ + PEG (Na^+:H_2O = 1:4.6)	*	10	VHCF	WO_3	60	1 A g^{-1}	1000	PEG-Na^+ complex	*	55
		2 M $NaClO_4/H_2O$ + DMSO	*	0.11 (50 °C)	AC	$NaTi_2(PO_4)_3$@C	100	1 C	100	*	Carbon layer	56
		$NaClO_4/H_2O$ + urea + DMF	1.53–4.33	8.1	Prussian blue analog (NiHCF)	$NaTi_2(PO_4)_3$	50	2 C	2000	*	Na_2CO_3	57
		2 M $NaNO_3$/60 wt. % maltose + H_2O	1.17–5.1	8.536	Sodium Prussian blue	AC	75	2 A g^{-1}	2000	*	*	53
		2 m $NaClO_4$/DMSO:H_2O (1:1)	1.33–4.48	*	$Na_3V_2(PO_4)_3$	$Na_3V_2(PO_4)_3$	90	585 mA g^{-1}	300	*	*	58
Alkali metal ion vs K/K^+	High concentration	$K(PTFSI)_{0.12}(TFSI)_{0.08}(OTf)_{0.8}$ $2H_2O$	2.15–4.65	34.6	*	*	*	*	*	*	*	118
		0.5 M K_2SO_4/H_2O	*	*	$K_2Fe^{II}Fe^{II}(CN)_6{\cdot}2H_2O$	Graphite	111	500 mA g^{-1}	500	*	*	120
		40 m KAc + 9.8 m LiAc·$2H_2O/H_2O$	1.91–4.76	8.0	$LiMn_2O_4$	AC	30	2 A g^{-1}	3000	*	K_2CO_3	37
		22 M KOTf/H_2O	1.86–4.86	76	$Fe_yMn_{1-y}[Fe(CN)_6]_w{\cdot}zH_2O$	PTCDI	60	4 C	2000	*	*	59
		40 M HCOOK/H_2O	0.64–4.64	46	*	$KTi_2(PO_4)_3$	15	0.1 A g^{-1}	*	*	*	60
		20 m KAc/H_2O	1.89–4.64	22.3	KMHCF	$KTi_2(PO_4)_3$	15	*	400	K_2CO_3	*	61
		67 m KFSI + KOTf/H_2O	2.05–4.75	12	$KVPO_4F$	$NaTi_2(PO_4)_3$	*	*	*	*	*	9
		21 m KOTf/H_2O	2.06–4.86	61.2	Iron hexacyanoferrate	$KTi_2(PO_4)_3$/C	40	5 A g^{-1}	30 000	*	*	62
		20 m KOTf + 30 m KFSI/H_2O	*	*	Prussian blue analogues KMnHCF nanocubes	$KTi_2(PO_4)_3$/C	70	1 A g^{-1}	3000	*	*	121

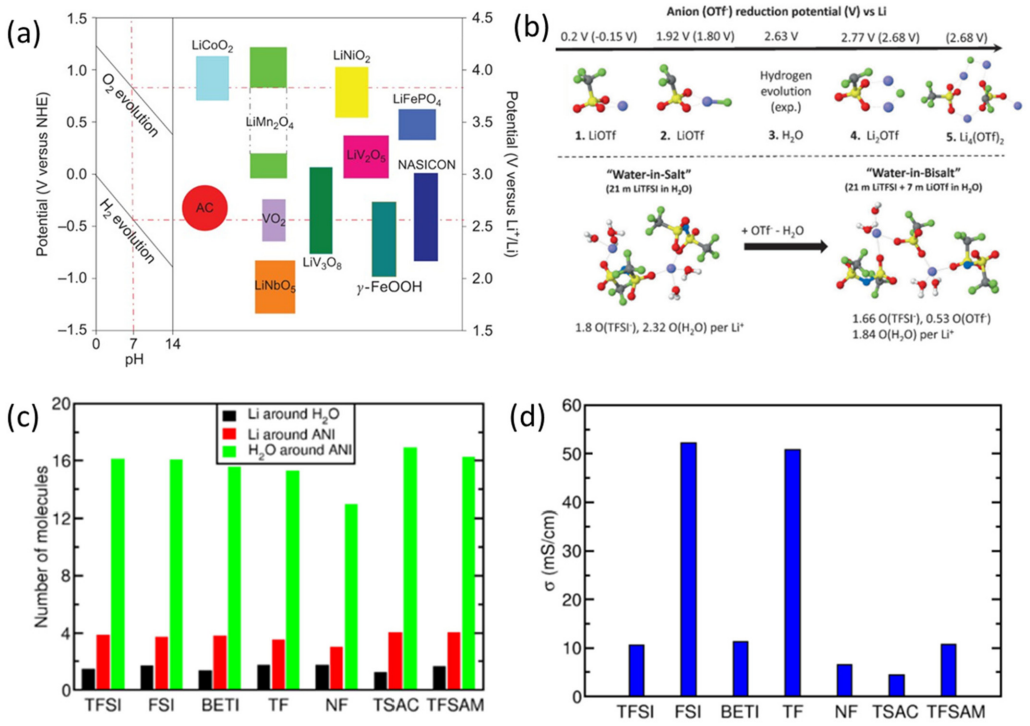

FIG. 3. (a) Intercalation potential for selected electrode materials for aqueous lithium-ion batteries. Reproduced with permission from Luo *et al.*, Nat. Chem. **2**, 760 (2010). Copyright 2010 Springer Nature.[31] (b) Upper: reduction stability for LiOTf complexes vs Li/Li^+ from quantum chemistry (QC) and DFT (in parentheses) computation with implicit water model; lower: schematic for Li^+ solvation structure evolution with addition of 7 m LiOTf. Reproduced with permission from Suo *et al.*, Angew. Chem., Int. Ed. Engl. **55**, 7136 (2016). Copyright 2016 Wiley.[18] (c) Neighbor count around reference subset (subsets are defined to match three (3) types of molecules, anions, water, and lithium) from Voronoi analyses for differing WIS electrolytes. (d) Comparison of ionic conductivity of WIS electrolytes at room temperature. Reproduced with permission from Mendez-Morales *et al.*, Batteries Supercaps **4**, 646–652 (2020). Copyright 2020 Wiley.[32]

To resolve the "cathodic challenge," an "inhomogeneous additive" method was used in which hydrophobic 1,1,2,2-tetrafluoroethyl-20,20,20-trifluoroethyl ether (HFE) additive[34] was reported to repel water molecules from electrode surface and decompose into a complex SEI with inorganic LiF//organic fluorides. In consequence, a 4.0 V high-voltage aqueous LIB was created via coupling $LiVPO_4F$ with graphite in gel-WIBS, and formation of SEI confirmed by the disappearance of the peak at ~0.7 V in the third CV, together with a capacity reduction from the charge/discharge voltage profile [Fig. 4(c)]. Importantly, the high-cost of Li salts, including LiOTf, LiTFSI, and LiBETI, restricts practical application. A superconcentrated aqueous electrolyte with low-cost $LiNO_3$ salt[35] was discovered that exhibited an ESW of 2.55 V because of unique electrolyte structure where $(Li^+(H_2O)_2)_n$ polymer-like chains replace ubiquitous hydrogen bonding between water molecules with increase in concentration, as displayed in Fig. 4(d). In addition to improvements in ESW and SEI, the high concentration strategy was reported to lead to new reaction pathways on a sulfur cathode. The electrochemical behavior of sulfur in WIBS and non-aqueous electrolyte are compared in Fig. 4(e).[36] Unlike the two-stage conversion of "sulfur—high-order polysulfide—low-order sulfide solid" in non-aqueous electrolyte, the lithiation of sulfur undergoes phase change from a high order polysulfide to low-order polysulfides through solid–liquid two-phase reaction pathway in the WIBS (21 m LiTFSI + 7 m LiOTf) electrolyte. The Li//sulfur battery with the WIBS electrolyte exhibited, therefore, a high energy density of 200 W h kg^{-1} and a high-capacity retention of 86% following 1000 cycles. Except for Li salts for WIBS electrolyte, a low-cost superconcentrated (SC) aqueous electrolyte with potassium acetate (KAc) and lithium acetate (LiAc)[37] was discovered with broadened ESW and high capacity for activated carbon (AC)//$LiMn_2O_4$ (LMO) aqueous lithium-ion hybrid electrochemical supercapacitors (L-HECs). As presented in Fig. 4(f), the ESW for SC electrolyte is increased from 1.9 to 2.85 V, benefiting from high K^+ concentration to confine water molecules via intense cation solvation. Furthermore, the suppressed freezing point for SC electrolyte allows L-HECs to work within an increased temperature range to exhibit energy and power densities of 77.9 W h kg^{-1} and 149.1 W kg^{-1} at 60 °C.

2. Hybrid solvents

Although a significant increase in ESWs was confirmed via formation of anion-originated SEI in WIS and WIBS electrolytes, a further improvement in a cathodic limit is practically difficult because of repulsion of anions by a negatively polarized anode surface. As the electrode surface is polarized to 0.50 V and lower, the anions undergo increasing expulsion from the surface and a significant fraction of water molecules adsorb with hydrogens pointing toward the surface, making SEI formation disrupted by HER. Because of this, many of the

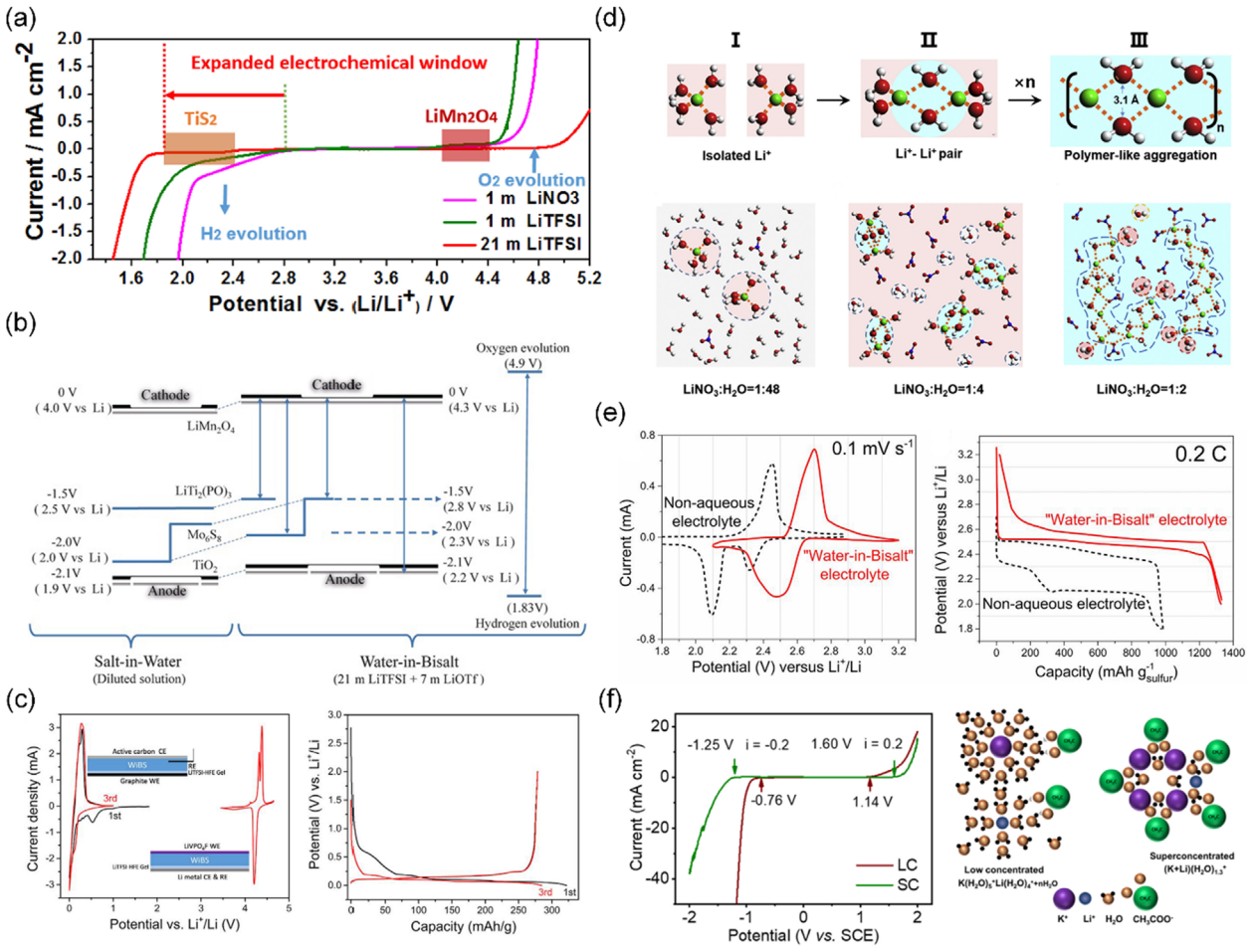

FIG. 4. High concentration strategy for ALIBs. (a) ESWs for 1 m $LiNO_3$, 1 m LiTFSI, and 21 m LiTFSI electrolytes. Reproduced with permission from Sun *et al.*, Electrochem. Commun. **82**, 71 (2017). Copyright 2017 Elsevier.[33] (b) Output voltage produced by electrochemical couples: $LiMn_2O_4$//$LiTiPO_4$, $LiMn_2O_4$//Mo_6S_8, and $LiMn_2O_4$//TiO_2. Reproduced with permission from Suo *et al.*, Angew. Chem., Int. Ed. Engl. **55**, 7136 (2016). Copyright 2016 Wiley.[18] (c) ESWs and charge/discharge profiles for LiTFSI-HFE gel-coated graphite electrode. Reproduced with permission from Yang *et al.*, Joule **1**, 122 (2017). Copyright 2017 Elsevier.[34] (d) Solvation structure for Li^+ in aqueous $LiNO_3$ solution with increasing concentration. Reproduced with permission from Zheng *et al.*, Chem **4**, 2872 (2018). Copyright 2018 Elsevier.[35] (e) Electrochemical performance for sulfur–Ketjen black carbon (S-KB) composite electrode in aqueous and nonaqueous electrolytes. Reproduced with permission from Yang *et al.*, Proc. Natl. Acad. Sci. U. S. A. **114**, 6197 (2017). Copyright 2017 National Academy of Sciences.[36] (f) ESWs and cation solvation for SC and low-concentration (LC) electrolytes. Reproduced with permission from Deng *et al.*, Energy Storage Mater. **20**, 373 (2019). Copyright 2018, Elsevier.[37]

energy-dense anode materials cannot be supported sufficiently by WIS and WIBS electrolytes, and only anode materials with moderate lithiation potential, including Mo_6S_8 (2.3 and 2.8 V), fall into the ESW. Even LTO anode with a redox potential of 1.55 V within the 1.9 V cathodic limit of the WIBS electrolyte (21 m LiTFSI + 7 m LiOTf) does not operate reversibly over the long term or operate to its full capacity, unless its surface is coated with an artificial interphase.[38]

Therefore, to increase the limit for WIS and WIBS electrolytes for high energy density of ALIBs, efforts were made via hybridizing aqueous and non-aqueous solvents. The introduction of organic solvent advantageously widened ESW and extended liquid range for electrolyte under low temperatures and *in situ* formation of functional SEI/CEI. Particularly, as presented in Fig. 5(a), the 14 M LiTFSI in dimethyl carbonate (DMC)-H_2O hybrid solvents exhibit a significant cathodic limit of 1.0 V and high anodic potential of 5.1 V and accommodates the redox reactions of $Li_4Ti_5O_{12}$ and $LiNi_{0.5}Mn_{1.5}O_4$ cathodes (4.96/4.82 V). Additional increasing of ESW was made via a hybrid "bisolvent-in-salt" electrolyte (BSiS) with the addition of co-solvent acetonitrile (AN).[22] The ESW for the BSiS–AN hybrid electrolyte was significantly increased to 4.5 V (0.7–5.2 V vs Li/Li^+) in Fig. 5(b) because of the double-layer SEI that is made of nitrile (C≡N) and sulphamide (R–S–N–S) species based organic outer layer and LiF-rich inner layer. In addition, this electrolyte exhibits a low freezing point of −48 °C and enables a $LiMn_2O_4$//$Li_4Ti_5O_{12}$ full cell with excellent cycling stability and rate capability at both 25 °C and 0 °C. Other non-aqueous solvents, including water–miscible polymer poly(ethylene glycol)(PEG), were reported with excellent ability to expand the ESW at low concentration. As can be seen in Fig. 5(c), 2 m

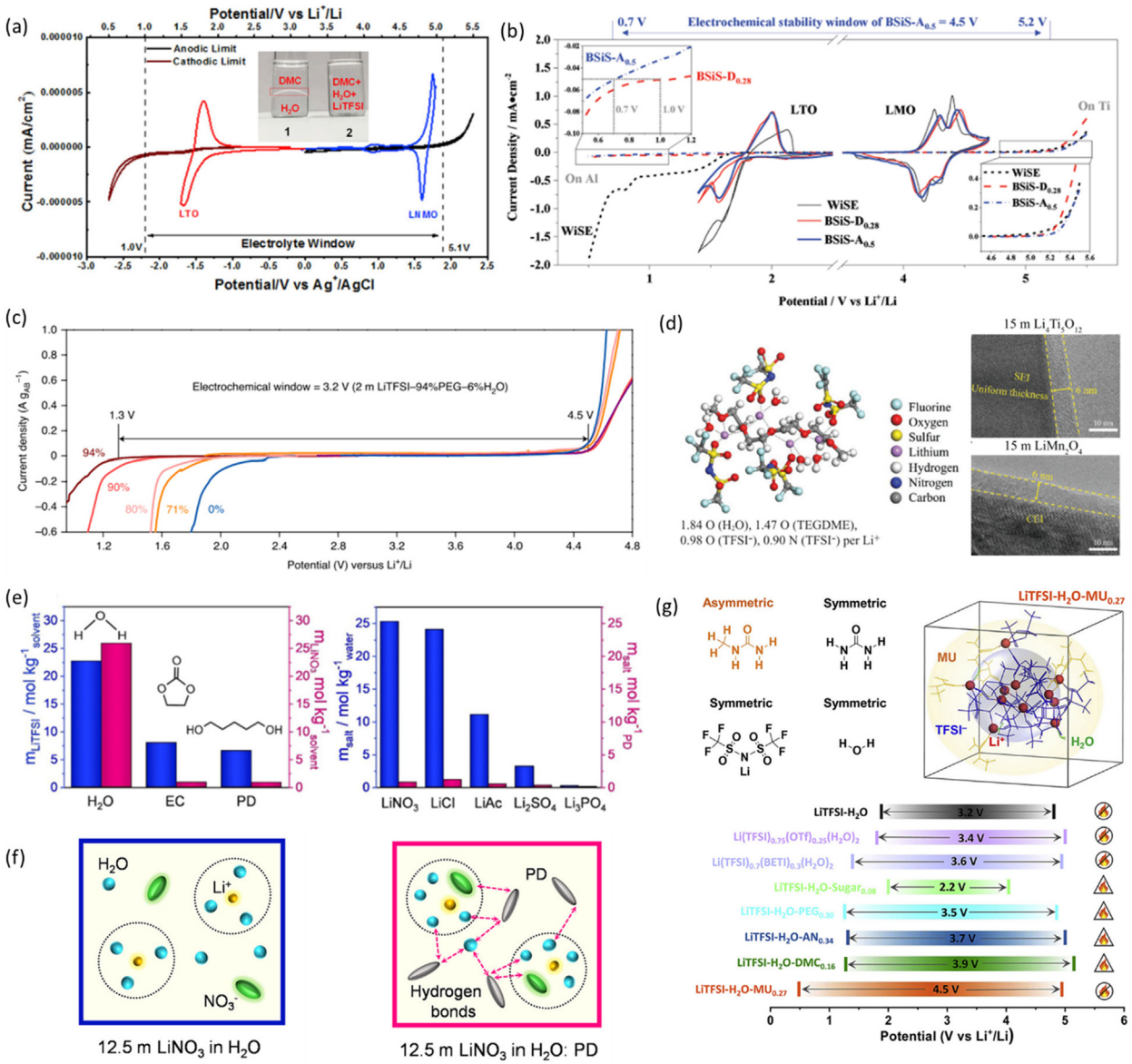

FIG. 5. Hybrid solvents strategy for ALIBs. (a) ESW for 14 M LiTFSI-DMC-H_2O electrolyte determined with CV on current collectors (cathodic and anodic limits were separately tested using Al and Pt as working electrodes and AC and Ag/AgCl as counter and reference electrodes, respectively) together with active electrodes, spinel $Li_4Ti_5O_{12}$, and $LiNi_{0.5}Mn_{1.5}O_4$.[38] (b) ESWs for WISE, BSiS-$D_{0.28}$ (Li^+/water/DMC molar ratio = 1:1.43:0.55), and BSiS-$A_{0.5}$ (Li^+/water/AN molar ratio = 1:1.11:1.11) electrolyte and CVs for LTO and LMO in these electrolytes. Reproduced with permission from Chen *et al.*, Adv. Energy Mater. **10**, 1902654 (2019). Copyright 2019 Wiley.[22] (c) ESWs for 2 m LiTFSI–xPEG–(1 − x) H_2O (x = 0%, 71%, 80%, 90%, and 94%). Reproduced with permission from Xie *et al.*, Nat. Mater. **19**, 1006 (2020). Copyright 2020 Springer Nature.[39] (d) Schematic for Li^+ first coordination shell (left) and TEM images (right) of LTO and LMO surfaces. Reproduced with permission from Shang *et al.*, Adv. Mater. **32**, e2004017 (2020). Copyright 2020 Wiley.[17] (e) Left: solubilities for $LiNO_3$ (pink) and LiTFSI (blue) in a selected solvent; Right: solubility for selected salts in water (blue) and PD (pink) at 25 °C. (f) Illustration of 12.5 m $LiNO_3$ in H_2O and 12.5 m in H_2O:PD and LWIS gel electrolyte. Reproduced with permission from Jaumaux *et al.*, Angew. Chem., Int. Ed. Engl. **60**, 19965 (2021). Copyright 2021 Wiley.[23] (g) Upper: Solvation structure of LiTFSI-H_2O-$MU_{0.27}$ electrolyte; lower: comparison of ESWs for selected electrolytes. Reproduced with permission from Lin *et al.*, Joule **6**, 399 (2022). Copyright 2022 Elsevier.[40]

LiTFSI–94%PEG–6%H_2O[39] electrolyte exhibits an ESW of 3.2 V (1.3–4.5 V), confirming a stable specific energy between 75 and 110 W h kg^{-1} with $Li_4Ti_5O_{12}$//$LiMn_2O_4$ full cells over 300 cycles. Other types of solvent including ether is considered as an excellent co-solvent because of low viscosity, high ionic conductivity, and capability of forming thin, compact, and uniform interphase(s). An "ether-in-water" electrolyte (EIWE) was reported via introducing TEGDME[17] into a concentrated aqueous electrolyte forming a novel

$Li_4(TEGDME)(H_2O)_7$ solvation structure [Fig. 5(d)]. Consequently, a new carbonaceous component for both cathode and anode–electrolyte interface was generated, as evidenced by TEM in Fig. 5(d), where even and stable 6 nm SEI and 6 nm CEI were found on the surface of $Li_4Ti_5O_{12}$ and $LiMn_2O_4$ following the first cycle. Because of electrode/electrolyte interphase protection preventing the electrode from side reactions, the electrochemical performance for $Li_4Ti_5O_{12}$//$LiMn_2O_4$ full cell was optimized. Different to salt soluble solvents, the inert diluent was reported to increase the ESW of electrolyte by forming locally concentrated water-in-salt (LWIS) electrolyte. In particularly, 1,5-pentanediol (PD)[23] in Fig. 5(e) is a good diluent as the solubility of LiTFSI and $LiNO_3$ in PD is much less than that in H_2O and ethylene carbonate (EC). By introducing the PD diluent into a 25 m $LiNO_3$-H_2O WIS electrolyte at a solvent mass ratio of 1:1 (H_2O:PD) to decrease the concentration to 12.5 m, the original solvation structure of WIS was maintained [Fig. 5(f)]. With *in situ* polymerization of tetraethylene glycol diacrylate (TEGDA) in the LWIS electrolyte, an ESW of 3.0 V was exhibited for the LWIS gel electrolyte. Another LWIS with highly significant 0.5 V cathodic limit was demonstrated via asymmetric methylurea (MU) molecules[40] which possess both donor and acceptor functional groups for forming "peculiar" nanoscale core-shell-like clusters. The core-shell-like clusters presented as Fig. 5(g) enabled localized concentrated electrolyte (LiTFSI-H_2O-$MU_{0.27}$) to exhibit a stable operation of NbO_2 anode with a 70% increase in energy density as compared with $Li_4Ti_5O_{12}$.

3. Eutectic solvents

Despite advantages with the WIS electrolyte of broadened ESW compared with dilute electrolyte and ability for anion-derived SEI, it still cannot compete with commercialized organic electrolytes on cost and energy density. Some hybrid electrolytes using organic solvents, including DMC and AN, have safety risks in aqueous batteries. Therefore, assessing dilute aqueous electrolytes that meet the following criteria are demanded: a wide ESW, low-cost, and non-flammability. Regarding these, the eutectic electrolyte via using a selected component to form a ternary eutectic with salts and H_2O was developed. Deep eutectic solvents are an emerging class of mixtures that contain hydrogen bond donors and hydrogen bond acceptors, and they have gain much attention due to merits of structural flexibility, good chemical stability, wide ESWs, low freezing point, and high vapor pressure. Conventional hydrogen bond donors include amide, alcohol, amine, amino acid, sugar, or carboxylic acid, while urea and N-methyl acetamide are components of choice for electrolyte application due to their safety and availability. The salts with hydrogen bond acceptors, such as LiTFSI, LiOTf, and $LiClO_4$, are reported as good eutectic electrolyte components. Eutectic electrolytes with distinguished properties could be optimized by selecting the hydrogen bond donors/acceptors and adjusting their ratios.[41]

A novel 4.5 m LiTFSI–KOH–$CO(NH_2)_2$–H_2O non-flammable ternary eutectic electrolyte[6] with an ESW of >3.3 V (1.5–4.8 V) was reported. In this electrolyte, $CO(NH_2)_2$ works as a model diluent and KOH is a catalyst for SEI formation. Introduction of $CO(NH_2)_2$ into the electrolyte corresponds to a $Li(CO(NH_2)_2)_{2.5}(H_2O)_{0.7}(TFSI)_{0.8}$ solvation structure where the Li^+ solvation is coordinated with $CO(NH_2)_2$, and water is reduced in the Li^+ primary solvation shell [Fig. 6(a)]. The coordination number for $CO(NH_2)_2$, TFSI, and H_2O around Li^+ for 4.5 m electrolyte and 21 m WISE in Fig. 6(b) shows that $CO(NH_2)_2$ serves as extra Li^+ ion coordinate site and takes the place of water in the solvation sheath. This unique structure led to a robust LiF/polymer bilayer SEI as evidenced by the predicted reduction potential for differing Li^+ complexes in Fig. 6(c). Because of significantly higher reduction potential for Li_2TFSI complex, LiTFSI preferably decomposes to LiF before polymerization of $CO(NH_2)_2$. The formation mechanism and components for this robust bilayer SEI illustrated in Fig. 6(d) where the inner LiF-dominant inorganic layer is from the decomposition of $TFSI^-$ and the outer layer are electrochemically polymerized polyurea.

An increased ESW of 3.5 V was reported with a novel deep eutectic solvents (DES) electrolyte[42] that consisted of methylsulphonylmethane (MSM), $LiClO_4$, and H_2O, as shown in Figs. 6(e)–6(f). By controlling components in a ratio of 1.8:1:1 (MSM:$LiClO_4$:H_2O, denoted as DES-1 electrolyte), a high conductivity of 3.87 mS cm^{-1} at room temperature, and a low melting point of −48 °C were achieved. By way of comparison, the DES-1 electrolyte exhibits significant advantage for accommodating LMO and LTO electrodes because of wider ESW over the 21 M WIS and 1 M $LiClO_4$ electrolyte, as seen in Figs. 6(g) and 6(h). Using the same salt, another DES composed of $LiClO_4 \cdot 3H_2O$ and urea with a molecular ratio of 1:2 (denoted as 1–2 electrolytes)[27] was demonstrated with an ESW of ∼3.2 V [Fig. 6(i)]. The Li^+ primary solvation shell in Fig. 6(j) illustrates that compared with the dilute 1 M $LiClO_4$ + 1 M urea electrolyte, most water molecules are coordinated with Li^+ in 1–2 electrolytes, and limited urea molecules were observed in the primary solvation sheath of Li^+. As a result, the 2.2 V $Li_4Ti_5O_{12}$//$LiMn_2O_4$ battery using 1–2 electrolytes and graphene coated Al current collector exhibited a long cycle life of >1000 cycles and a high energy density of 135 W h kg^{-1}.

In addition to improvements with ESW, electrode/electrolyte interphases were built with a $LiClO_4$ salt based eutectic electrolyte. With a $LiClO_4$–H_2O–urea ratio of 1–3–2, a novel $[Li(H_2O)_x(organic)_y]^+$ solvation sheath is constructed which was confirmed to be critical to SEI formation on $LiMn_2O_4$ cathode and Mo_6S_8 anode. The TEM image of Fig. 6(k) evidences that the $LiMn_2O_4$ is covered by 10–25 nm thick imperfect crystalline Li_2CO_3 derived from urea and capable of suppressing Mn dissolution and OER. The SEI layer (composed of stable hydrophobic polyurea and Li_2CO_3 generated from the reduction in oxygen and CO_2 dissolved in electrolyte) on Mo_6S_8 anode [Fig. 6(l)] protects the anode by isolating it from active water.[43]

4. Ionic liquid and water-in-salt hybrid

The apparent success with highly concentrated electrolyte boosted development of mixtures, such as IL and WIS hybrid electrolytes, which dissolves more salt than the sole WIS electrolyte because of the presence of ILs. When the water solvent is substituted with ILs, the electrolyte exhibits boosted ionic conductivity, low viscosity, and an expanded ESW.

It was demonstrated that RT ionic liquids (RTILs) exhibit hydrotropic effect that boosts salt solubility and does not act through micellar solubilization. To exploit this hydrotropic effect of RTILs, 1-ethyl-3-methylimidazoliumTFSI (EMImTFSI) was mixed with WIS electrolyte to boost solubility of LiTFSI from 21 to 60 mol kg^{-1}.[44] To establish the influence of hydrophobic EMImTFSI and hydrophilic EMImtrifluoromethanesulphonate (EMImOTf) on the solubility of

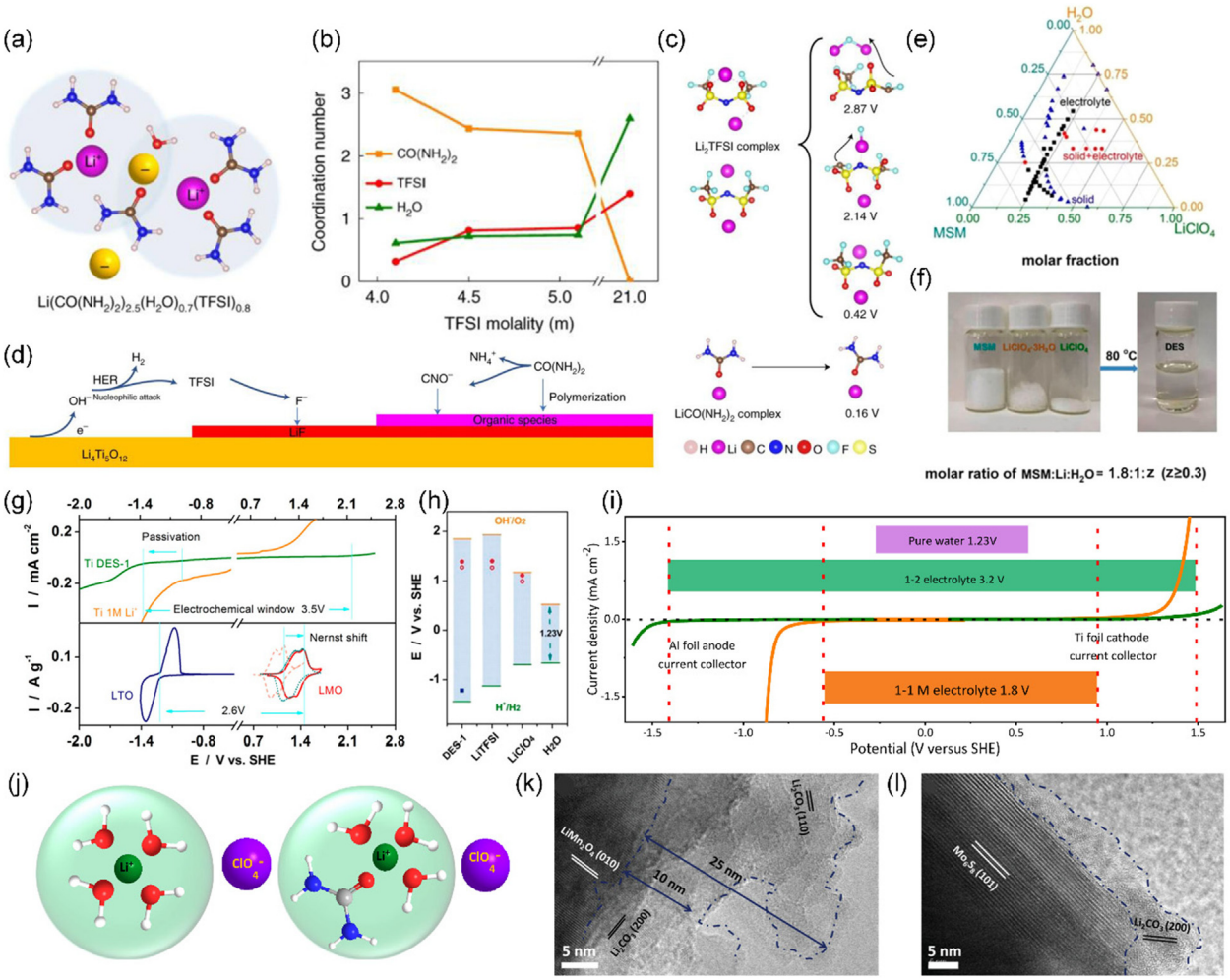

FIG. 6. Eutectic solvents strategy for ALIBs. (a) Scheme for Li^+ primary solvation shell in 4.5 m electrolyte. (b) Coordination number for $CO(NH_2)_2$, TFSI, and H_2O around Li^+. (c) Predicted reduction potential from DFT computation. (d) Illustration for formation of organic/inorganic SEI. Reproduced with permission from Xu *et al.*, Nat. Energy **7**, 186 (2022). Copyright 2022 Springer Nature.[6] (e) Ternary phase diagram for mMSM-n$LiClO_4$-zH_2O salt–water mixture. (f) Preparation of DES-0.3 (MSM:$LiClO_4$:H_2O = 1.8:1:0.3). (g) ESW of DES-1 and CVs for LMO and LTO electrodes. (h) Expanded ESWs for DES-1 and LiTFSI (21 M) and formal potentials for LMO and LTO in DES-1, LiTFSI, $LiClO_4$, and pure water. Reproduced with permission from Jiang *et al.*, ACS Energy Lett. **4**, 1419 (2019). Copyright 2019 American Chemical Society.[42] (i) ESWs for selected aqueous electrolyte. (j) Primary solvation sheath structure for Li^+ in 1–1 M (left) and 1–2 (right) electrolyte. Reproduced with permission from Zhang *et al.*, Energy Storage Mater. **46**, 147 (2022). Copyright 2022 Elsevier.[27] TEM images of (k) $LiMn_2O_4$ and (l) Mo_6S_8 following 10 cycles under $LiClO_4$–H_2O–urea electrolyte. Reproduced with permission from Hou *et al.*, Adv. Energy Mater. **10**, 1903665 (2020). Copyright 2020 Wiley.[43]

salts in WIS electrolyte, the differential scanning calorimetry (DSC) was carried to determine the water-to-lithium ratio in the electrolyte [Fig. 7(a)]. Compared with 21 m LiTFSI electrolyte with a water-to-LiTFSI ratio of 2.65, the ratio in 40 m LiTFSI and 20 m RTIL (sample 40/20) was significantly reduced to 1.39, and further increasing LiTFSI and LiOTf to near the solubility limit reduced the water-to-salt ratio but resulted in low ionic conductivity and large viscosity. Ternary phase diagrams for LiTFSI/RTIL/water in Fig. 7(b) show the region where extra solubility is exhibited, evidencing that RTILs can act as a solubility booster for LiTFSI in water. An optimized 40/20-TFSI (40 m LiTFSI in 20 m EMImTFSI) electrolyte exhibited excellent reduction and oxidization potential of 0.8 and 4.7 V, respectively.[44]

An additional isolated WIS solvation structure was proposed with IL 1-methyl-1-propylpiperidinium bis(fluorosulphonyl)imide ($PP_{13}FSI$)[30] as illustrated in Fig. 7(c). Hydrophobic PP_{13}^+ cations and lithium-philic FSI^- anions separate different H_2O–Li^+–FSI^- solvation clusters to significantly weaken the interaction between water molecules and give a significant ESW of 4.9 V (0.8–5.7 V). Moreover, this electrolyte leads to a uniform alkaline-based organic–inorganic SEI, which favors high Li^+ conductivity and suppresses HER, on $Li_4Ti_5O_{12}$ as illustrated in Fig. 7(d). Although there is significant progress on IL and WIS hybrid electrolytes, the molecular origin for this kind of electrolyte is not understood. Recent research via MD simulation evidence that the introduction of EmimTFSI into WIS (20 m LiTFSI) results in

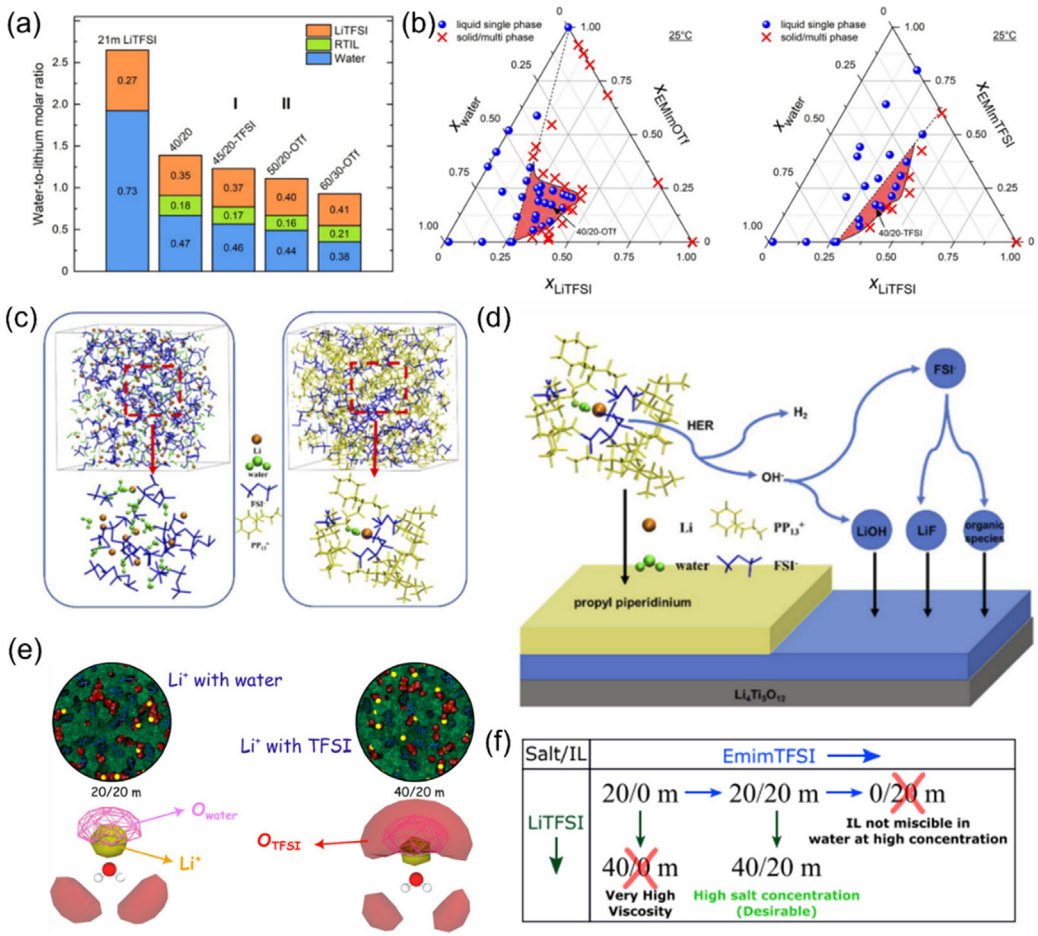

FIG. 7. Ionic liquid and WIS strategy for ALIBs. (a) Ratio between H_2O and Li in electrolytes. (b) Ternary phase diagram for LiTFSI/RTIL/water mixtures with EMImOTf (left) and EMImTFSI (right). Reproduced with permission from Becker *et al.*, Angew. Chem., Int. Ed. Engl. **60**, 14100 (2021). Copyright 2021 Wiley.[44] (c) Solvation structure for 28 m LiFSI (left) and 1LiFSI–4PP_{13}FSI–2H_2O (right). (d) Formation of inorganic–organic mixed SEI layer on the LTO electrode. Reproduced with permission from Zhang *et al.*, J. Mater. Chem. A **10**, 20545 (2022). Copyright 2022 The Royal Society of Chemistry.[30] (e) Microscopic structure of LiTFSI-EmimTFSI-based electrolytes. (f) Concentration of salt and IL used in WIS-IL hybrid mixture. Reproduced with permission from Dhattarwal and Kashyap, J. Phys. Chem. B **126**, 5291 (2022). Copyright 2022 American Chemical Society.[45]

the removal of water from the nearest neighbor solvation shell of $TFSI^-$ ions, but not from the Li^+ ions, as seen in Fig. 7(e). This structure confirms that boosted LiTFSI solubility with RTIL originates from the replacement of water molecules with $TFSI^-$ ions in the first solvation shell of Li^+ ions. It was, therefore, concluded that EmimTFSI could be used for a targeted high concentration of 40 m LiTFSI [Fig. 7(f)].[45]

III. AQUEOUS SODIUM- AND POTASSIUM-ION BATTERIES

A. Electrolyte strategies for aqueous sodium-ion batteries

Electrolyte strategies that can accommodate high-capacity electrode materials within the ESWs are needed for ASIBs. Among cathode materials for ASIBs, $Na_{0.44}MnO_2$ and $Na_3V_2(PO_4)_3$ exhibit the greatest practically promising performance for voltage and capacity when used with $NaTi_2(PO_4)_3$ anode in 1 M Na_2SO_4 electrolyte. $Na_{0.44}MnO_2$//$NaTi_2(PO_4)_3$ exhibits a high energy density of 33 W h kg^{-1} with charge/discharge rates > 100 C and capability to be cycled > 1000 times. $Na_3V_2(PO_4)_3$//$NaTi_2(PO_4)_3$ has an energy density of 29 W h kg^{-1} and power density of 5145 W kg^{-1}. Figure 8(a) presents the redox potential for selected electrode materials and ESWs for electrolytes, e.g., hybrid aqueous/nonaqueous, WIS, and dilute aqueous. WIS strategies for ASIBs, including the use of 9.26 m NaOTf in H_2O with an ESW of 2.6 V, are practically useful for extending ESW close to the performance of hybrid aqueous/nonaqueous electrolytes, such as 7.5 m NaOTf in H_2O/propylene carbonate (PC) with ESW of 2.8 V. Strategies using concentrated electrolytes permit increased selection of cathodes and anodes for ASIBs, while keeping stable cycling behavior following formation of the protective interphase layer. Figure 8(b) shows use of DFT to assess reduction potentials for differing NaOTf complexes. It is seen in the figure that the

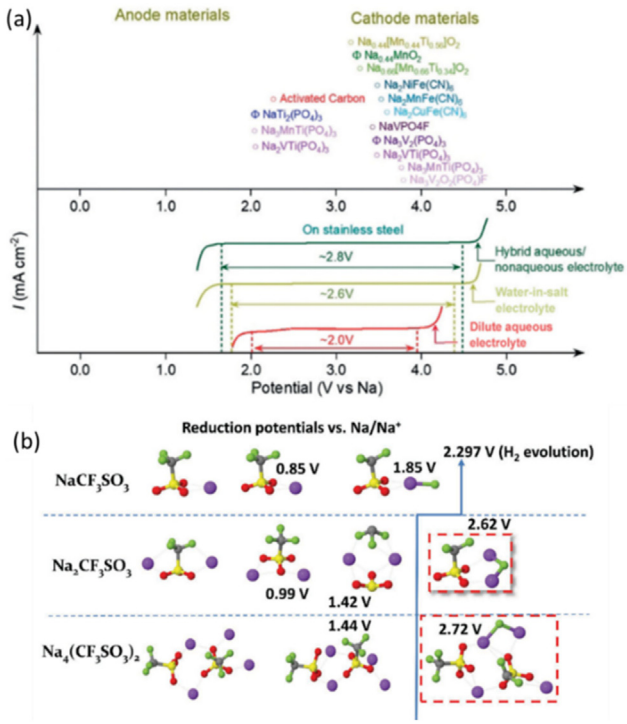

FIG. 8. (a) Average redox potentials of electrode materials (upper) and ESWs of hybrid aqueous/nonaqueous, water-in-salt, and dilute electrolytes (down) for ASIBs. Reproduced with permission from Zhang *et al.*, Angew. Chem., Int. Ed. Engl. **60**, 598 (2021). Copyright 2020 Wiley.[46] (b) Reduction potentials for three NaOTf complexes [$NaCF_3SO_3$, $Na_2CF_3SO_3$, and $Na_4(CF_3SO_3)_2$] from QC computation. Reproduced with permission from Suo *et al.*, Adv. Energy Mater. **7**, 1701189 (2017). Copyright 2017 Wiley.[47]

reduction of Na_2OTf and $Na_4(OTf)_2$ to form NaF can be achieved at potential higher than that for HER. A significant gap between 0.3 and 0.4 V above the HER potential is practically "ideal" because this protects the anode via formation of NaF on the surface, suppressing water decomposition and H_2 evolution. Judiciously combined assessments using MD give insight that low salt concentration of 9.0 m is sufficient for formation of respective NaOTf complexes and reduction to form a protective NaF layer.

Progress in design was made on a sodium-ion WIS electrolyte (NaWISE) which exhibits a 2.5 V ESW with HER suppressed by NaF-based SEI. A primary solvation sheath in "salt-in-water" (SIW) disappears because of insufficient water molecules and, therefore, the SIW solution is considered a liquefied salt [Fig. 9(a)]. Understanding some critical differences between Li-ion and Na-ion WISE is important. A more pronounced contact ion pairs (CIP, NaOTf)/aggregated cation–anion pairs (AGGs, $Na_nOTf)^{(n-1)+}$ in NaOTf–H_2O electrolyte account for formation of SEI in NaWISE with relatively low salt concentration compared with that for lithium-ion WIS electrolyte (LiWISE).[47] LSV curves for aqueous electrolytes evidence that the introduction of 2 m NaOTf into 17 m $NaClO_4$ [Fig. 9(b)] expands the ESW for 19 m bi-salts WISE to 2.8 V. The robust SEI composed of NaF, Na_2O, and NaOH is generated from reduction of OTf^- preventing water decomposition and enabling $Na_3V_2(PO_4)_3$ (NVP) anode with a low potential of 1.70 V to exhibit a 1.75 V symmetric NVP@C// NVP@C full cell with a high energy density of 70 W h kg^{-1}.[48] WISE for 32 m KAc and 8 m NaAc (32K8Na) significantly extends cathodic limit to < -2.0 V (vs Ag/AgCl) and OER is not apparent with Al or Ti electrode in Fig. 9(c). Practically, promising electrochemical performance of Al-foil loaded $Na_2MnFe(CN)_6$ (NMHCF) and $NaTi_2(PO_4)_3$/C (NTP/C) electrodes is demonstrated by high symmetry and reproductivity of CVs in 32K8Na electrolyte, underscoring advantage of fluorine-free, WISE.[49] When the water-to-salt molar ratio is <2, the NaFSI based aqueous electrolyte exhibits high stability and a wide ESW of 2.6 V, meaningfully greater than that for 21 m LiTFSI [Figs. 9(d) and 9(e)]. Reversible behavior of $NaTi_2(PO_4)_3$ anode and $Na_3(VOPO_4)_2F$ cathode in 35 m NaFSI confirms the feasibility and superiority of proposed 35 m NaFSI electrolyte for high-voltage ASIB.[50] A "dense and thick" SEI generated in concentrated 8 m $NaClO_4$ and 9.26 m NaOTf prevents dissolution of vanadium species from NASICON-type $Na_2VTi(PO_4)_3$ electrode. This is evidenced by the color of separator from cells following cycling that separators in WISE keep white in color while separator in diluted 1 M $NaClO_4$ becomes yellow-color [Fig. 9(f)].[51] Commonly used salts for WISE, including Na_2SO_4, $NaNO_3$, and $NaClO_4$ are to be compared in solubility, cost, and solvation strength. Saturated, designed 17 m $NaClO_4$ contributes to formation of a passivation film composed of Na_2CO_3 and NaOH on the $NaTi_2(PO_4)_3$ surface [Fig. 9(g)]. The dense interlayer results in $Na_4Fe_3(PO_4)_2(P_2O_7)$//$NaTi_2(PO_4)_3$ full-cell with significant stability.[52] A low-cost WIS aqueous electrolyte of 26 m NaTFA exhibits a wide ESW of 3.1 V and a high ionic conductivity of 23 mS cm^{-1}. A robust fluoride layer forms in the electrolyte as illustrated in Fig. 9(i), ensuring a stable ESW and accelerating redox reaction of $V^{2+/3+/4+}$ and $Ti^{3+/4+}$ in NASICON-type $Na_2VTi(PO_4)_3$.[8]

A hybrid superconcentrated sugar-based electrolyte exhibits an ionic conductivity of 8.536 mS cm^{-1}, liquid range of –50 to 80 °C, and ESW of 2.812 V. This can be attributed to concentrated sugar, including decreasing free water, breaking the original hydrogen bonds (H-bonds) between water molecules, and serving as solvent for dissolving concentrated salts. Consequently, superconcentrated sugar-based electrolytes have a significantly widened ESW compared with reported electrolytes, as seen in Fig. 10(a)[53] and Table I. An additional hybrid aqueous NaOTf electrolyte with addition of PC exhibited a highly significant high ionic conductivity of 25 mS cm^{-1} at 20 °C and an increased ESW of 2.8 V [Fig. 10(b)].[54] A design progress was made with low-cost salt electrolyte using PEG and water as mixed solvents. A complex of PEG with Na^+ (PEG–Na^+) was observed on the vanadium hexacyanoferrate (VHCF) surface that boosted stability of VHCF and facilitated alkali-ion transfer [Fig. 10(c)].[55] Because of low melting point and capability for forming H-bond with water molecules, as illustrated in Fig. 10(d), dimethyl sulphoxide (DMSO) is added to 2 m $NaClO_4$ aqueous solution to obtain a hybrid 2M-0.3 electrolyte with an ultra-low freezing point of <-130 °C and good ionic conductivity of 0.11 mS cm^{-1} at −50 °C, resulting in a $NaTi_2(PO_4)_3$@C(NTP) || 2 M-0.3 || AC battery with excellent rate and cycle performance at −50 °C in Fig. 10(e).[56] Beyond binary solvents, a multicomponent aqueous electrolyte (MCAE) composed of sodium perchlorate, urea, N,N-dimethylformamide (DMF) and water was assessed. The low field shift for Na–H_2O–urea–DMF in ^{23}Na NMR spectroscopy [Fig. 10(f)] confirmed an ion shielding effect of urea and DMF that reduced viscosity and increased ionic conductivity of the

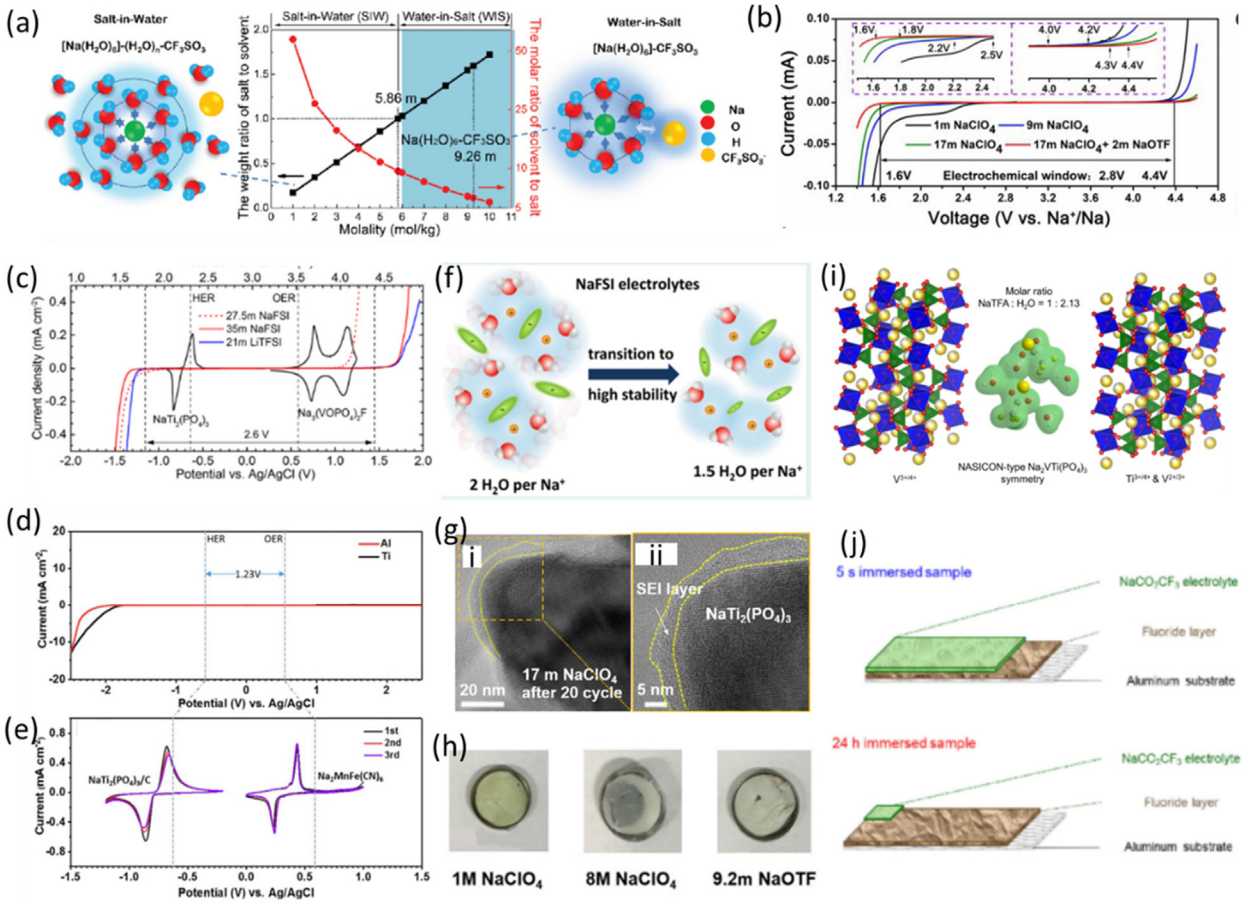

FIG. 9. High concentration strategy for ASIBs. (a) Molar and mass salt/solvent ratio in NaOTf–H_2O electrolyte. Reproduced with permission from Suo *et al.*, Adv. Energy Mater. **7**, 1701189 (2017). Copyright 2017 Wiley.[47] (b) ESWs for 1 m $NaClO_4$, 9 m $NaClO_4$, 17 m $NaClO_4$, and 17 m $NaClO_4$–NaOTf. Reproduced with permission from Jin *et al.*, Angew. Chem., Int. Ed. Engl. **60**, 11943 (2021). Copyright 2021 Wiley.[48] (c) LSV recorded in 32K8Na electrolyte and CV for NMHCF and NTP/C coated on Al-foil. Reproduced with permission from Han *et al.*, ChemSusChem **11**, 3704 (2018). Copyright 2018 Wiley.[49] (d) Solvation structure for NaFSI based aqueous electrolytes. (e) ESWs for electrolyte and CVs for $Na_2MnFe(CN)_6$ cathode and $NaTi_2(PO_4)_3$/C anode. Reproduced with permission from Kühnel *et al.*, ACS Energy Lett. **2**, 2005 (2017). Copyright 2017 American Chemical Society.[50] (f) Photograph of separators following 1000 cycles. Reproduced with permission from Zhang *et al.*, ChemSusChem **11**(8), 1382–1389 (2018). Copyright 2018 Wiley.[51] (g) TEM analyses of $NaTi_2(PO_4)_3$ anode. Reproduced with permission from Lee *et al.*, Mater. Today **29**, 26 (2019). Copyright 2019, Elsevier.[52] (h) Reversible symmetrical operation of NASICON-type $Na_2VTi(PO_4)_3$ with 26 m NaFSI electrolyte. (j) Schematic for XPS spectra evidencing that top layer is mainly NaTFA and next layer NaF. Reproduced with permission from Nakamoto *et al.*, Electrochemistry **89**, 415 (2021). Copyright 2021 Authors, licensed under a Creative Commons Attribution (CC BY) license.[8]

MCAE. The MCAE has a wide ESW of 2.8 V [Fig. 10(g)].[57] With addition of DMSO, HER onset potential for 2 m $NaClO_4$–H_2O–DMSO is decreased from −0.6 to −1.6 V (vs Ag/AgCl) allowing conversion between V^{2+} and V^{3+} (−1.2 V vs Ag/AgCl) prior to HER [Fig. 10(h)]. It is concluded, therefore, that $Na_3V_2(PO_4)_3$ exhibits maximum discharge capacity with transition between multivalent state ($V^{2+} \leftrightarrow V^{3+} \leftrightarrow V^{4+}$) in Fig. 10(i).[58]

B. Electrolyte strategies for aqueous potassium-ion batteries

A 22 M KOTf WIS electrolyte with a wide ESW enables K^+ to intercalate into 3,4,9,10-perylenetetracarboxylic di-imide (PTCDI) anode prior to HER. The expanded ESW and ability to inhibit PTCDI anode dissolution are attributed to the strong K^+-solvation effect inducing decreased free water content. A "sharp" peak at 3531 cm^{-1} in the Raman spectra in Fig. 11(a) confirms strong K^+-solvation effect.[59] An environmental-friendly and low-cost concentrated 40 M HCOOK electrolyte with a water-to-salt molar ratio of 1.38: 1 was reported for APIB. The potential window is expanded to 4 V (−2.5 to 1.5 V vs Ag/AgCl) in Fig. 11(b).[60] The gradually increased ESW for KAc with increasing concentration was obtained with Al-foil and Pt-foil in Fig. 11(c). Compared with Pt, the electrolyte exhibited a higher OER potential and lower HER potential with Al current collector. This was explained by progressive passivation of Al-foil in anodic scan and inferior HER electrocatalytic performance of Al itself. The XPS spectra of cycled and pristine electrode confirm SEI formation and degradation of active potassium manganese hexacyanoferrate (KMHCF) material [Fig. 11(d)].[61]

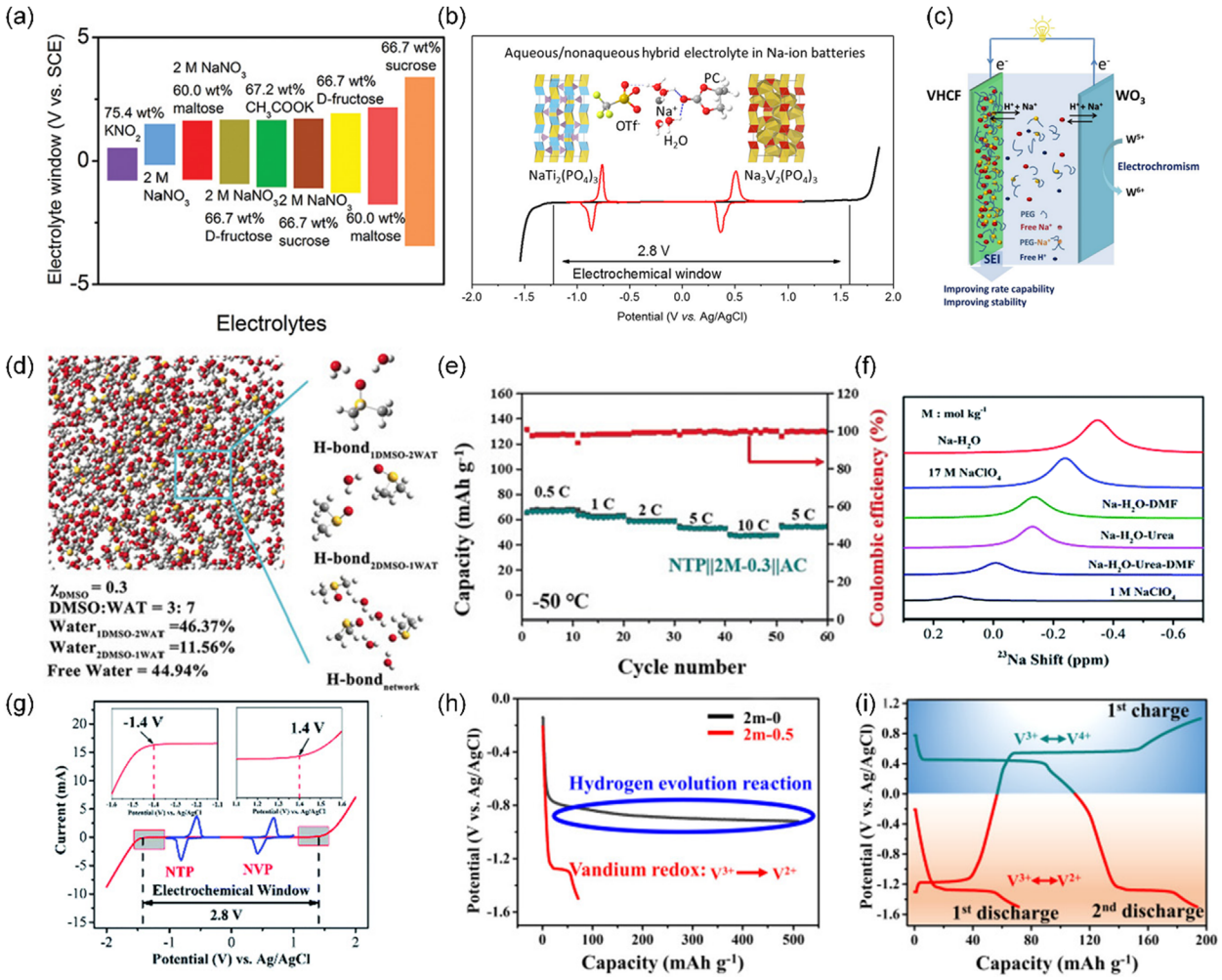

FIG. 10. Additive and co-solvent strategy for ASIBs. (a) ESWs for selected low-concentration and superconcentrated solutions. Reproduced with permission from Bi *et al.*, Adv. Mater. **32**, e2000074 (2020). Copyright 2020 Wiley.[53] (b) Hybrid electrolyte based on NaOTf with ESW of 2.8 V. Reproduced with permission from ACS Energy Lett. **3**, 1769 (2018). Copyright 2018 American Chemical Society.[54] (c) Rechargeable aqueous sodium-ion battery (VHCF//WO_3) with electrolyte of PEG/H_2O/$NaClO_4$. Reproduced with permission from ACS Appl. Mater. Interfaces **11**, 28762 (2019). Copyright 2019 American Chemical Society.[55] (d) Conformation analysis of $\chi_{DMSO} = 0.3$ system. (e) Rate performance for full battery with 2 M-0.3 electrolyte at −50 °C. Reproduced with permission from Angew. Chem., Int. Ed. Engl. **58**, 16994 (2019). Copyright 2019 Wiley.[56] (f) ^{23}Na NMR spectra for selected electrolytes. (g) ESW for Na–H_2O–urea–DMF electrolyte. Reproduced with permission from J. Mater. Chem. A **8**, 14190 (2020). Copyright 2020 The Royal Society of Chemistry.[57] (h) Discharge curve for NVP in 2 m-0 (black) and 2 m-0.5 (red). (i) Charge-discharge profile for NVP in 2 m-0.5. Reproduced with permission from ACS Energy Lett. **6**, 2174 (2021). Copyright 2021 American Chemical Society.[58]

A "rocking-chair" type aqueous $KTi_2(PO_4)_3$/C//K-FeHCF full K-ion battery with a WIS electrolyte of 21 m KOTf was designed as shown in Fig. 11(e). The concentrated 21 m KOTf provided an ESW of 2.8 V, greater than that for 1 m KOTf of 2.1 V. The superconcentrated 21 m electrolyte envelops the voltage window for K^+ insertion/extraction, which enables K-FeHCF//$KTi_2(PO_4)_3$/C full cell with a high capacity retention of 96.7% over 30 000 cycles.[62] A K-ion aqueous electrolyte composed of KFSI and KOTf with an ultra-high K^+ concentration of 61.7 m was designed without sacrificing ionic conductivity. The liquidus phase diagram of Fig. 11(f) shows that a K-ion molality of 61.7 m is exhibited at a eutectic point for $K(FSI)_{0.55}(OTf)_{0.45}$. The upward Raman shift for $K(FSI)_{0.55}(OTf)_{0.45}{\cdot}0.9H_2O$[9] evidences the formation of CIPs and AGGs via the coordination between $[FSI]^-$ and K^+, and a sharp peak that is characteristic of crystalline hydrate is observed. This structure evidences that clustered water molecules are fully disassembled and coordinated with ionic species. As a result, the 61.7 m electrolyte exhibits a wide 2.7 V potential window on Pt and among the widest reported for all alkali-ion aqueous electrolytes.

IV. AQUEOUS ZINC METAL BATTERIES

A. Solid electrode interphases on the Zn metal anode

In AZIBs, the SEI has attracted particular interest due to the function of extending the stable operational range of the aqueous

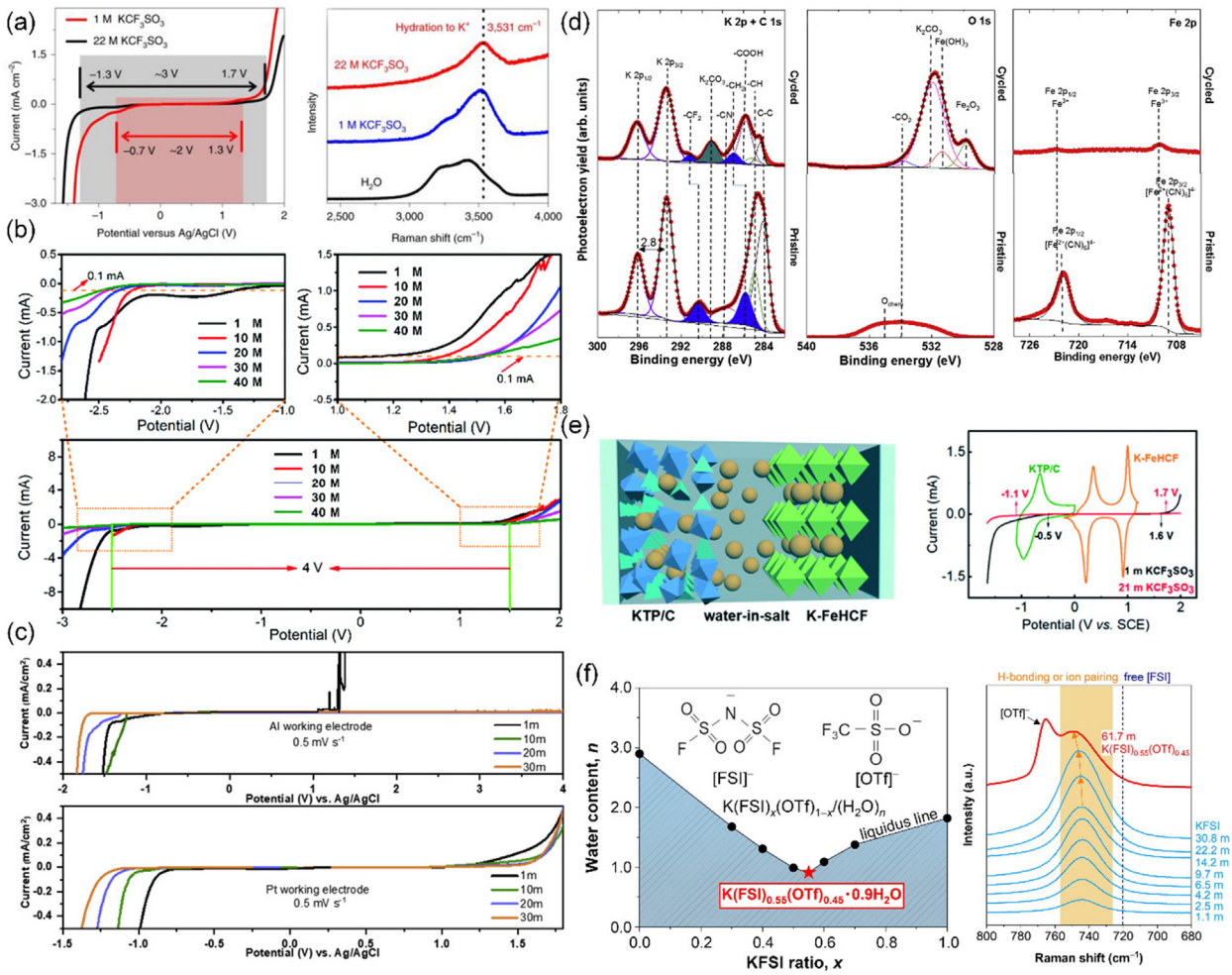

FIG. 11. Electrolyte strategy for APIBs. (a) ESWs and Raman spectra for 1 M and 22 M KOTf electrolytes. Reproduced with permission from Nat. Energy **4**, 495 (2019). Copyright 2019 Springer Nature.[59] (b) ESWs for HCOOK electrolytes. Reproduced with permission from Chem. Commun. (Cambridge, U. K.) **55**, 12817 (2019). Copyright 2019 The Royal Society of Chemistry.[60] (c) LSV curves for selected KAc electrolytes determined with Al and Pt as working electrodes. (d) XPS spectra for cycled and pristine KMHCF electrodes. Reproduced with permission from Energy Storage Mater. **30**, 196 (2020). Copyright 2020 Elsevier.[61] (e) Scheme for KTP/C || WIS || K-FeHCF AFKIB and ESWs of 1 m and 21 m KOTf electrolytes. Reproduced with permission from J. Mater. Chem. A **9**, 2822 (2021). Copyright 2021 The Royal Society of Chemistry.[62] (f) Liquidus phase diagram for $K(FSI)_x(OTf)_{1-x}/(H_2O)_n$ (left) and Raman spectra (right) for $K(FSI)_{0.55}(OTf)_{0.45}{\cdot}0.9H_2O$ and KFSI/H_2O solutions. Reproduced with permission from Electrochem. Commun. **116**, 106764 (2020). Copyright 2020 Elsevier.[9]

electrolyte and alleviating zinc dendrite growth. Constructing robust SEI with high ionic conductivity can effectively improve the zinc reversibility, which is critical for achieving high zinc anode utilization and long battery cycling life. Given the importance of SEI in extending ESW and protecting the anode, design strategy has been directed to hybrid solvents, additives and eutectic solvents to construct *in situ* SEI in AZMBs (Fig. 12). Unlike ALIBs that favor LiF compounded protective interphase, SEI development in AZMBs has only emerged in recent years. On SEI composition, a number of inorganic and organic compounds have been developed using the preceding design strategies (Table II) that address unwanted dendrites, but which had not been systematically summarized. Currently, ZnF_2, $ZnCO_3$, and $Zn_3(PO_4)_2$ are generally accepted as good SEI components because of high electronic insulation and good Zn^{2+} conductivity. A co-solvent PC based hybrid electrolyte[63] generates a hydrophobic $ZnCO_3$–ZnF_2 SEI via anion reduction, enabling uniform Zn plating and inhibiting Zn dendrite formation. A hopeite SEI [$Zn_3(PO_4)\cdot4H_2O$][11] synthesized from an additive strategy is reported with good, lower electronic conductivity of $\sigma = 1.1 \times 10^{-8}$ S cm^{-1} and lower activation energy of 33.4 kJ mol^{-1} compared with bare Zn anode, offering rapid Zn^{2+} transport highways and enabling fast desolvation kinetics through the layer. Additionally, the structure for SEI is equally important. For example, a bilayer morphology, robust inorganic ZnF_2–$Zn_5(CO_3)_2(OH)_6$–organic bilayer,[64] and a monolithic SEI[65] were reported to functionally promote Zn^{2+} diffusion in ZnF_2-$Zn_5(CO_3)_2(OH)_6$ inner layer and to suppress water penetration in the organic, outer layer.

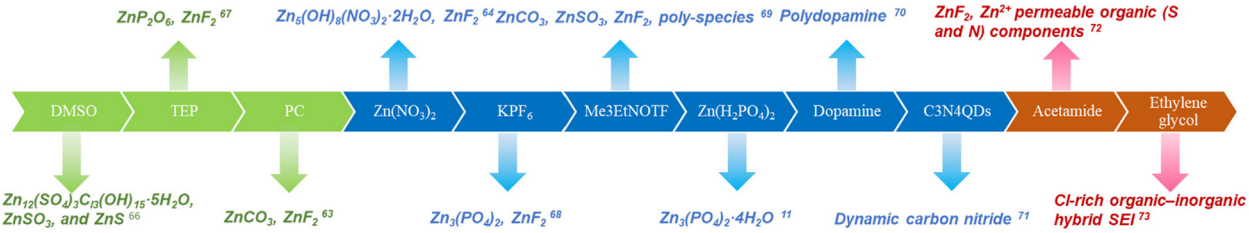

FIG. 12. Compositions of electrode/electrolyte interphases for zinc metal protection derived from hybrid solvent (green-color bars), additives (blue), and eutectic solvents (orange) electrolyte strategies.[11,63,64,66–73] The main component of these electrolytes, e.g., organic co-solvent, additives, and eutectic solvent, is displayed in each bar, while the generated SEI is listed under or below the bar.

B. Developments in advanced electrolyte strategies

1. High concentration

The high crustal abundance of Zn with high volumetric capacity of 5854 Ah l^{-1} and gravimetric capacity of 820 mAh g^{-1}, together with the compatibility of Zn with mild and non-flammable aqueous electrolytes, makes AZMBs a practical competitor for complementary solutions to LIBs.[74] Dendritic Zn deposition ubiquitous in alkaline electrolytes is (almost) eliminated in applying neutral pH electrolytes, and therefore, adoption of mild electrolyte improves cyclability of AZMBs.[75,76] Several mild Zn salt electrolytes, including zinc sulfate ($ZnSO_4$), zinc triflate [$Zn(OTf)_2$], zinc chloride ($ZnCl_2$), and zinc acetate [$Zn(Ac)_2$], have been used widely in AZMBs. However, the aqueous electrolyte used is susceptible to temperature change, causing it to freeze at sub-zero that leads to degradation, or failure, of batteries. Therefore, good temperature adaptability of aqueous electrolytes is a crucial requirement. The altered anions cause significant changes in the overall physicochemical properties of the aqueous electrolyte of Zn salts. For example, in $Zn(OTf)_2$ solutions the weak interaction of OTf^- with Zn^{2+} and H_2O, respectively, gives a strong interaction of Zn^{2+} with H_2O. By selecting anions with stronger interactions with Zn^{2+}, the coordination number between Zn^{2+} and H_2O decreases as the anion enters the solvated structure of Zn^{2+}, as shown in Fig. 13(a).[77] Based on this, Zhang *et al.*[77] systematically assessed the influence of a series of electrostatic potentials (ESP) for anions on the H-bond number in water clusters, and demonstrated that the order of the lowest ESP of the anion is consistent with the average number of H-bonds per water molecule in the different electrolytes [Fig. 13(b)]. Through combined experimental characterizations and MD simulation, the authors confirmed that strong interactions between anions with low ESP value and cations cause the anions to displace the water originally in the coordination shell of cations, resulting in weakening of the cation-induced H-bond breakage. This mechanism for anion-induced H-bond reduction assists understanding of temperature-adaptive electrolyte selection. Later, Yang *et al.*[78] demonstrated that the strong interaction of anions with water molecules facilitates disruption of H-bonds between pairs of water molecules. MD simulations evidence that Zn salts containing chaotropic anions (ClO_4^-) form H-bonds with H_2O and break the hydrogen bonding network of free water, thereby providing better low-temperature adaptation than Zn salts composed of kosmotropic anions (SO_4^{2-}), as shown in Fig. 13(c). In addition to the effect on temperature adaptation, the selection of the anion in Zn salt affects the stability of the Zn metal electrode. The strong interaction of the anion with Zn^{2+} decreases the coordination number for Zn^{2+} with H_2O. Based on this, Patil *et al.*[79] reported that $ZnSO_4$ solutions, in which the H_2O in the solvation sheath of Zn^{2+} is extruded by SO_4^{2-}, have more free water than $Zn(TFSI)_2$ solutions where the solvation sheath of Zn^{2+} contains no anions. Therefore, the $Zn(TFSI)_2$ solution with lower free water boosts cycling stability of the constructed Zn//Zn symmetric cells compared with $ZnSO_4$ solution.

Despite the widespread use of aqueous electrolytes, a major practical difficulty is the narrow ESW because of hydrolysis of water.[80] To address this, design strategies for regulation of salt concentration were developed. For example, suppressed Zn^{2+} hydrolysis is evidenced by decreased acidity of electrolyte with increasing of LiTFSI concentration in Fig. 13(e). In 1 m $Zn(TFSI)_2$ + 20 m LiTFSI electrolyte, Zn^{2+} is surrounded by $TFSI^-$ and the unfavorable generation of H^+ in deprotonation from aqua ions $(Zn(OH_2)_6)^{2+}$ to hydroxyl species $Zn(OH)_2$ or, ZnO, is hindered. The hybrid Zn//$LiMn_2O_4$ battery exhibits an excellent cycle performance with 85% capacity retention following 4000 cycles with a CE of 99.9%.[81] ESW for the electrolyte is widened from 1.6 to 2.3 V as the concentration of $ZnCl_2$ changes from 5 to 30 m [Fig. 13(f)].[82] In addition, intense interaction between water molecules and anions in concentrated electrolytes results in an electrolyte with anti-freezing property. The red-shift of the B–F bond with increased $Zn(BF_4)_2$ concentration confirms the intense interaction between water molecules and BF_4^- in Fig. 13(g). 4 M $Zn(BF_4)_2$ electrolyte with a freezing point of −122 °C and ionic conductivity of 1.47 mS cm^{-1} at −70 °C enabled a Zn//tetrachlorobenzoquinone (TCBQ) battery to operate at −95 °C.[83] A supersoluble $ZnCl_2$/$ZnBr_2$/$Zn(OAc)_2$ aqueous electrolyte with a record concentration of 75 m overcomes limited physical solubility. Nonpolarized protons in acetate anions prevent the overgrowth and precipitation of ionic oligomers, to give an anti-freezing electrolyte 45 m $ZnBr_{0.5}Cl_{1.5}$ + 1 m $Zn(OAc)_2$ water–salt oligomer electrolyte ($WSOE_{45}$-1) of $T_g \sim -70$ to −60 °C. The high discharge capacity and Coulombic efficiency (CE) exhibited by Zn/graphene fiber fabric (GFF) || $WSOE_{45}$-1 || graphene cathode (PGA) battery is attributed to a suppressed "shuttle effect" and improved intercalation of Br^- in the highly concentrated electrolyte [Figs. 13(h)–13(i)].[84]

2. Hybrid solvents

In addition to the regulation of salt type and concentration, a hybrid solvent synthesized from organic molecules and Zn salt solution is one of the most widely used electrolytes in AZMBs.

TABLE II. Aqueous Zn^{2+} ion batteries. (The symbol "∗" represents there is no data available from the referred work.)

	Electrolyte property			Full battery					Interphase(s)		
Electrolyte	Electrolyte	ESW	Ionic conductivity (mS cm^{-1})	Cathode	Anode	Capacity (mAh g^{-1})	Current rate	Cycling number	CEI	SEI	Ref.
Concentrated	3 M $Zn(ClO_4)_2/H_2O$	−2.5	4.23	V_2O_5	Zn	150	6 A g^{-1}	1000	∗	∗	78
	30 m $ZnCl_2/H_2O$	∗	28	∗	Zn	∗	∗	∗	∗	∗	82
	2 M $Zn(OTf)_2/H_2O$	−0.2–2.5	4.47 (−30 °C)	V_2O_5	Zn	208.7 (−30 °C)	0.5 A g^{-1}	1000	∗	∗	77
	4 M $Zn(TFSI)_2/H_2O$	−0.06–2.7	90	Poly(catechol) redox copolymer	Zn	274	10 C	12 500	∗	∗	79
	4 M $Zn(BF_4)_2/H_2O$	0.4–1.9	1.47 (−70 °C)	TCBQ	Zn	101.4 (−30 °C)	1 C	1000	∗	∗	83
	1 m $Zn(TFSI)_2$ + 20 m LiTFSI/H_2O	∗	∗	$Li_2Mn_2O_4$	Zn	30	4 C	4000	∗	∗	81
	4.2 M $ZnSO_4$ + 0.1 M $MnSO_4/H_2O$	∗	25.74	MnO_2	Zn	125	938 mA g^{-1}	1300	∗	ZnO	122
	45 m $ZnBr_{0.5}Cl_{1.5}$/1 m $Zn(OAc)_2/H_2O$	∗	1.28	PGA	Zn	605.7	1 A g^{-1}	500	∗	∗	84
Hybrid solvents	2.14 M $Zn(OTf)_2$ /H_2O + 50% PC	−1.9	16	$ZnMn_2O_4$	Zn	∗	350 mA g^{-1}	300	∗	$ZnCO_3$ and ZnF_2	63
	1 M $Zn(OTf)_2$/ DOL + H_2O	∗	30	V_2O_5	Zn	250	2 A g^{-1}	1500	∗	∗	87
	1.3 m $ZnCl_2$/DMSO + H_2O (volume ratio = 1:4.3)	∗	42.1	MnO_2	Zn	150	8 C	500	∗	$Zn_{12}(SO_4)_3C_{l3}(OH)_{15}{\cdot}5H_2O$, $ZnSO_3$, and ZnS	66
	0.5 M $Zn(OTf)_2$/TEP + H_2O	−2.2	∗	V_2O_5	Zn	250	5 A g^{-1}	100	∗	ZnP_2O_6, ZnF_2	67
	2 M $ZnSO_4$/40 vol. % EG/H_2O	2.8	6.9 (−40 °C)	PANI–V_2O_5	Zn	100	0.2 A g^{-1}	250	∗	∗	86
	2 M $ZnSO_4$/50 vol. % methanol/H_2O	2.4	16.8	PANI	Zn	130	5 A g^{-1}	2000	∗	∗	88
Additive	3 M $Zn(OTf)_2$ + 20 mM $Zn(NO_3)_2/H_2O$	∗	∗	MnO_2	Zn	145	10 C	700	∗	$Zn_5(OH)_8(NO_3{\cdot}2H_2O$ and ZnF_2	64
	0.05 M KPF_6 + 2 M $ZnSO_4/H_2O$	∗	∗	MnO_2	Zn	130	5 A g^{-1}	600	∗	$Zn_3(PO_4)_2$ and ZnF_2	68
	4 M $Zn(OTf)_2$ + 0.5 m $Me_3EtNOTf/H_2O$	−0.1–2.6	38.2	MnO_2	Zn	150	5 C	1000	∗	$ZnCO_3$, $ZnSO_3$, ZnF_2, and poly-species	69
	2 m $ZnSO_4$ + 0.1 m $MnSO_4/H_2O$	∗	∗	Ca_2MnO_4	Zn	100	1 A g^{-1}	1000	$CaSO_4{\cdot}2H_2O$	∗	93
	2 M $ZnSO_4$ + 0.05 M sodium glycerophosphate (SG, $C_3H_7Na_2O_6P$)/H_2O	∗	∗	PANI	Zn	110	5 A g^{-1}	1400	∗	$Zn_3(PO_4)_2$	123
	2 M $ZnSO_4$ + C_3N_4QDs/H_2O	−0.2	110	MnO_2	Zn	100	1 C	500	∗	Dynamic carbon nitride	71

TABLE II. (Continued.)

Electrolyte	Electrolyte property			Full battery					Interphase(s)		Ref.
	Electrolyte	ESW	Ionic conductivity (mS cm^{-1})	Cathode	Anode	Capacity (mAh g^{-1})	Current rate	Cycling number	CEI	SEI	
	1 M $Zn(OTf)_2$ + 50 mM DA /H_2O	*	*	V_2O_5	Zn	150	1 A g^{-1}	1000	*	PDA	70
	1 m $Zn(OTF)_2$ + 25 mM $Zn(H_2PO_4)_2$	*	*	V_2O_5	Zn	100	0.8 A g^{-1}	500	*	$Zn_3(PO_4)_2{\cdot}4H_2O$	11
Eutectic	30 mol. % H_2O in urea/ LiTFSI/$Zn(TFSI)_2$	2.5	1.85	$LiMn_2O_4$	Zn	65	2 C	600	*	*	95
	1:4 $ZnCl_2$/EG	2.15	1.15	PANI	Zn	100	2 A g^{-1}	10 000	*	Cl-rich organic–inorganic hybrid SEI	73
	1:7 $Zn(TFSI)_2$:acetamide	2.4	0.31	V_2O_5	Zn	110	600 mA g^{-1}	800	*	ZnF_2, Zn^{2+} permeable organic (S and N) components	72

These organic compounds regulate the solvation sheath structure of Zn^{2+} and guide interface formation.[65,85] Ming *et al.*[63] reported that a phase-separated PC/H_2O mixture is turned into a stable solution with assistance from hydrophobic $-CF_3$ group and hydrophilic $-SO_3^-$ on OTf^- [Fig. 14(a)]. The [PC–OTf^-–H_2O] amphipathic complex makes it possible for PC molecules to regulate Zn^{2+} solvation structure as PC is immiscible with water. Additionally, the protective interphase composed of $ZnCO_3$ and ZnF_2 generated from the reduction of OTf^- prevents the Zn anode from contacting water, achieving highly significant CE of 99.93% over 500 cycles for Zn//Cu asymmetric cell. It follows, therefore, that the organic additive selected be able to promote the formation of a dense solid electrolyte interface on the Zn surface to prevent corrosion and passivation. Cao *et al.*[66] suggested that the Gutmann donor number DN is an important criterion for selecting solvent additives. Because of the higher Gutmann donor number for DMSO (DN = 29.8 kcal mol^{-1}) and triethyl phosphate (TEP, DN = 26 kcal mol^{-1}) compared with that for H_2O (DN = 18 kcal mol^{-1}), the strong interaction between organic solvent and H_2O inhibits the decomposition of solvated H_2O and reduces water related unwanted side reactions. In Fig. 14(b), the thickness of deposited Zn is shown to be reduced from 10.9 to 6.5 μm when cycling in $ZnCl_2$–H_2O–DMSO, evidencing the efficacy of DMSO on inhibiting Zn dendritic growth. The $Zn_{12}(SO_4)_3Cl_3(OH)_{15}{\cdot}5H_2O$–$ZnSO_3$–ZnS interphase formed in $ZnCl_2$–H_2O–DMSO electrolyte also allows diffusion of Zn^{2+} and blocks water, resulting in an "even" Zn deposition and suppressed water related side reactions.

The nature of hybrid electrolytes allows them to meet practical needs. Electrolytes with anti-freeze properties have been reported by introducing anti-freeze organic additives. The widely used antifreeze, ethylene glycol (EG) is used to regulate the solvation structure of Zn^{2+} and decrease the freezing point of the hybrid electrolyte. H-bond between EG and H_2O is intensified, and solvation interaction between Zn^{2+} and H_2O is weakened, resulting in an ZMBs with an energy density of 121 W h kg^{-1} at -20 °C [Fig. 14(c)].[86] 1,3-dioxolane (DOL) with a fully exposed pair of electrons on the oxygen atom forms H-bond with water molecules and builds a new H-bond network. The binding energy for DOL–H_2O, DOL–$2H_2O$, and H_2O–H_2O are −2.662, −5.278, and 2.542 kcal mol^{-1}, respectively, underscoring the tendency for H_2O to combine with DOL [Fig. 14(d)]. The "trapped" H_2O molecules suppress HER and decomposition of water.[87] An interesting antisolvent strategy is to improve Zn reversibility with methanol. Formation of the homogeneous solution, followed by recrystallization of $ZnSO_4$ when adding methanol, confirms interaction between methanol, free water, and coordinated water in Zn^{2+} solvation sheath [Fig. 14(e)]. In this work, the strong adsorption of methanol on the surface of the Zn electrode and the strong interaction with free water together inhibit the hydrogel evolution reaction and broaden the potential window of the electrolyte, as shown in Fig. 14(f). Because water activity is minimized the electrochemical performance for the Zn//polyaniline (PANI) battery is significantly boosted at (extreme) temperatures of −20 and 60 °C.[88] In the $Zn(OTf)_2$–TEP–H_2O electrolyte, water molecules are forced out of the solvation sheath and the number of active water molecules decreases. During repeated charge/discharge, an interphase with improved electron insulating property composed of poly-metaphosphate and ZnF_2 is *in situ* generated from the decomposition of TEP and anions, obviating dendrite growth and parasitic reaction(s) [Fig. 14(g)].[67]

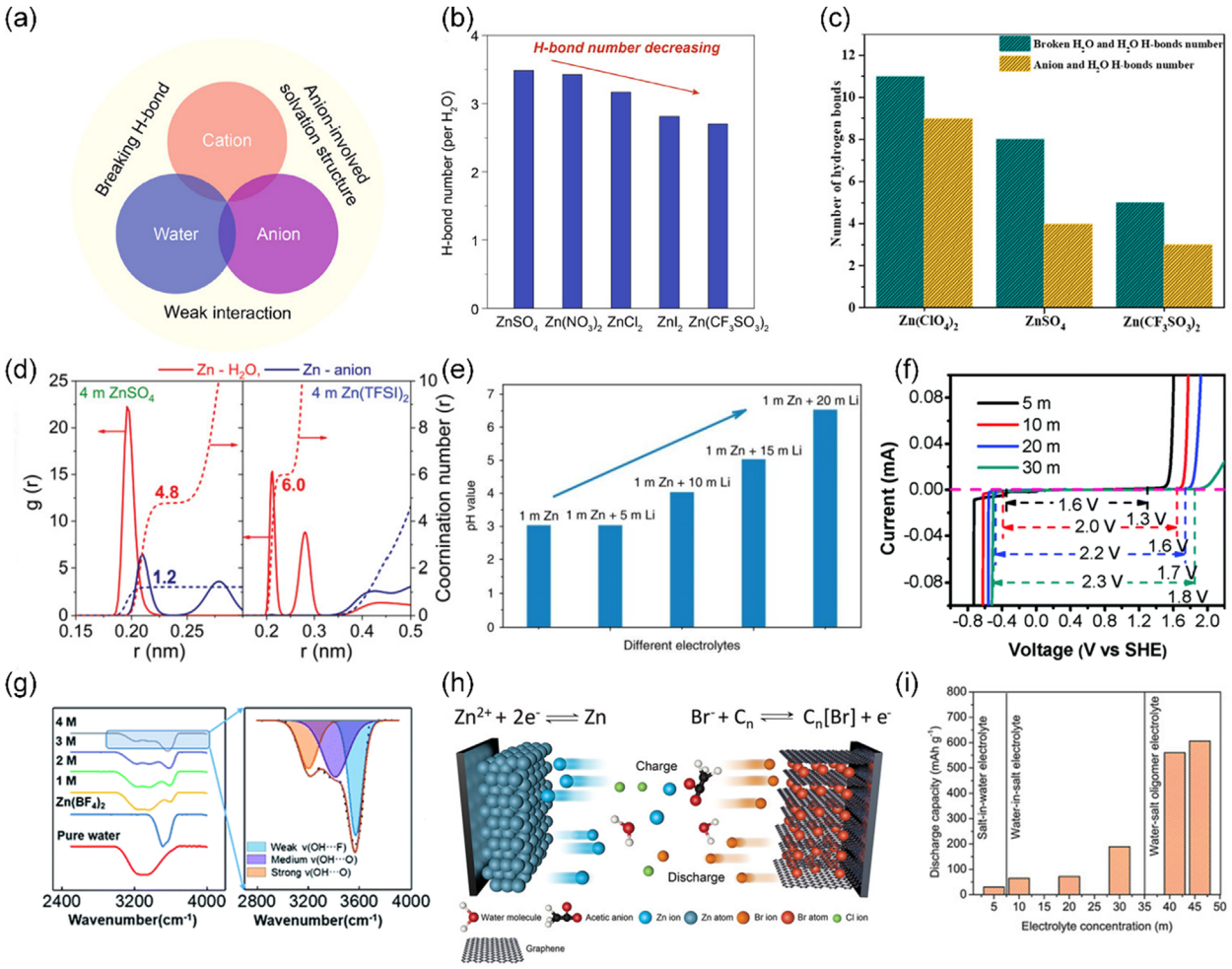

FIG. 13. High concentration strategy for AZMBs. (a) Schematic for cation–water, cation–anion, and anion–water interactions. (b) H-bond number for electrolytes with selected Zn salts in MD simulation. Reproduced with permission from ACS Energy Lett. **6**, 2704 (2021). Copyright 2021 American Chemical Society.[77] (c) H-bond number for $Zn(ClO_4)_2$, $ZnSO_4$, and $Zn(OTf)_2$ electrolytes. Reproduced with permission from EcoMat **4**, e12165 (2022). Copyright 2022 Wiley.[78] (d) Microscopic structure investigation of 4 m $ZnSO_4$ and 4 m $Zn(TFSI)_2$ via MD simulation. Reproduced with permission from Adv. Energy Mater. **11**, 2100939 (2021). Copyright 2021 Wiley.[79] (e) pH value for electrolyte with varying LiTFSI concentration. Reproduced with permission from Nat. Mater. **17**, 543 (2018). Copyright 2018 Springer Nature.[81] (f) ESWs for $ZnCl_2$ electrolyte of varying concentration. Reproduced with permission from Chem. Commun. (Cambridge, U. K.) **54**, 14097 (2018). Copyright 2018 The Royal Society of Chemistry.[82] (g) FTIR spectra for O–H bond in $Zn(BF_4)_2$ based electrolyte. Reproduced with permission from J. Mater. Chem. A **9**, 7042 (2021). Copyright 2021 The Royal Society of Chemistry.[83] (h) Schematic for Zn/GFF || $WSOE_{45}$-1 || PGA battery. (i) Discharge capacity for dual-ion battery with 5–46 m electrolyte. Reproduced with permission from Adv. Mater. **33**, e2007470 (2021). Copyright 2021 Wiley.[84]

3. Electrolyte additives

Adding of inorganic additives to electrolyte has been shown to be one of the effective methods to achieve controlled behavior of Zn plating. For example, graphitic carbon nitride quantum dots (C_3N_4QDs) have strong interaction with Zn^{2+} and regulate the solvation structure of Zn^{2+} as the $[Zn(C_3N_4)(H_2O)_4]^{2+}$ has the best binding energy [Fig. 15(a)]. Driven by Coulombic force, C_3N_4QDs are involved in dynamic construction and self-repairing of interphase on Zn surface during repeated stripping/plating without consumption. The regenerative interphase featuring zincophilic pores enables single Zn^{2+} ion conduction and blocks active water, leading to an even Zn deposit.[71] A stable $Zn_3(PO_4)_2{\cdot}4H_2O$ SEI *in situ* forms because of reaction between local water decomposition derived OH^- and the additive $Zn(H_2PO_4)_2$. DFT computation based on optimum Zn^{2+} diffusion pathway tagged from Zn0 to Zn6 in SEI evidences that the SEI enables rapid Zn^{2+} transportation [Fig. 15(b)]. Furthermore, Zn^{2+} diffusion energy barrier in a channel within SEI of 0.66 eV is relatively less than that for other multivalent-cations, such as Mg^{2+} diffusion in $FePO_4$[89] or V_2O_5,[90] confirming the superiority of designed SEI for ZMBs [Fig. 15(c)].[11] By adding a trace amount of $Zn(NO_3)_2$, robust inorganic ZnF_2-$Zn_5(CO_3(OH)_6$-$Zn(NO_3)_2)_2$-organic bilayer SEI is fabricated. The element distribution for SEI following 50 cycles of Fig. 15(d) shows that the dominant composition gradually changes from organic

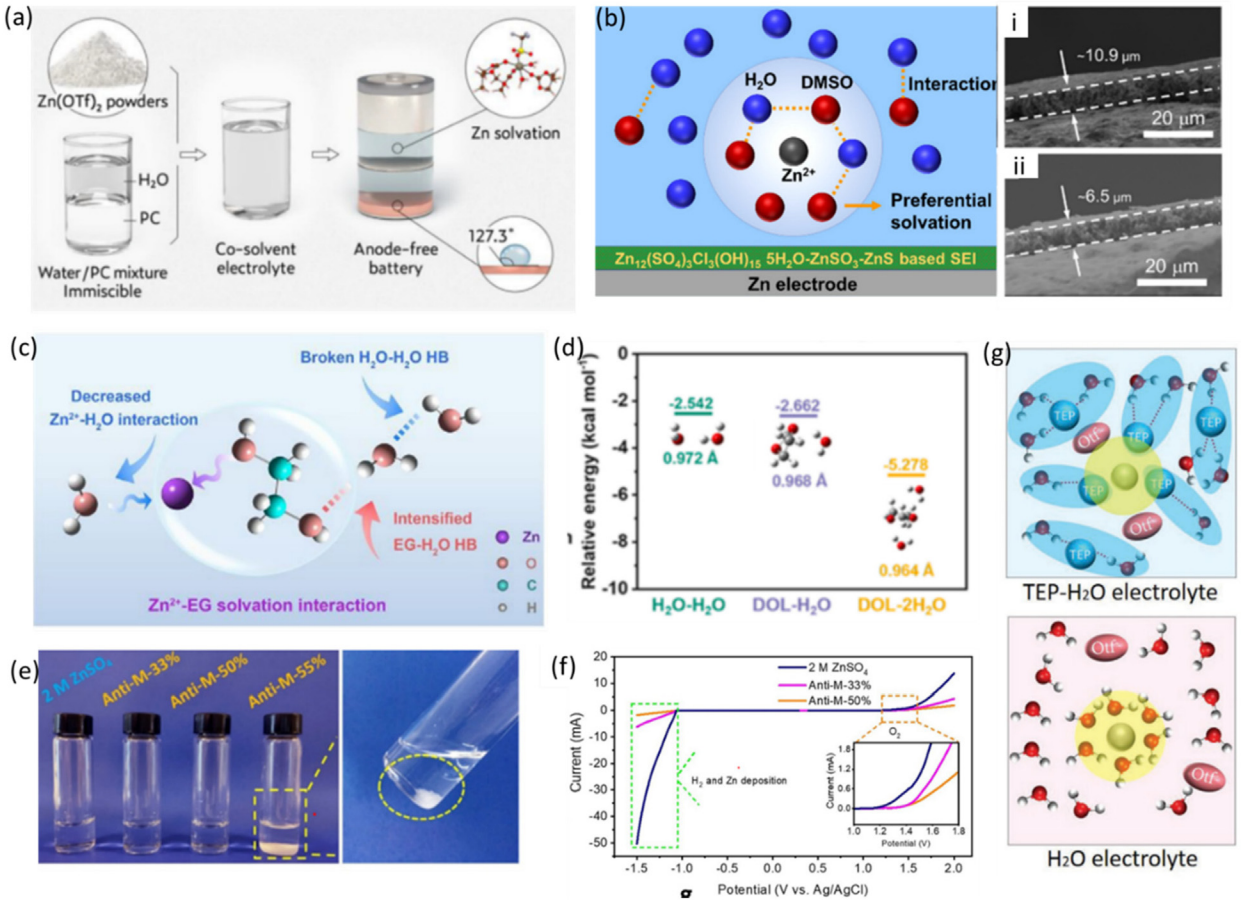

FIG. 14. Hybrid solvent strategy for AZMBs. (a) Preparation of hybrid PC/H_2O electrolyte and anode-free battery. Reproduced with permission from J. Am. Chem. Soc. **144**, 7160 (2022). Copyright 2022 American Chemical Society.[63] (b) Schematic for Zn^{2+} solvation structure and SEM image of Zn electrode cycled in $ZnCl_2$-H_2O and $ZnCl_2$-H_2O-DMSO electrolyte. Reproduced with permission from J. Am. Chem. Soc. **142**, 21404 (2020). Copyright 2020 American Chemical Society.[66] (c) Scheme for Zn^{2+}–EG interaction in the hybrid electrolyte. Reproduced with permission from Energy Environ. Sci. **13**, 3527 (2020). Copyright 2020 The Royal Society of Chemistry.[86] (d) DFT computation derived binding energy for H_2O–H_2O, DOL–H_2O, and DOL–$2H_2O$. Reproduced with permission from Chem. Eng. J. **427**, 131705 (2022). Copyright 2022 Elsevier.[87] (e) Preparation of methanol- and ethanol-based electrolytes. (f) LSV response curves for 2 M $ZnSO_4$ and methanol-based antisolvent electrolytes at 0.1 mV s^{-1}. Reproduced with permission from Angew. Chem., Int. Ed. Engl. **60**, 7366 (2021). Copyright 2021 Wiley.[88] (g) Scheme for Zn^{2+} solvation structure and generated interphases in $Zn(OTf)_2$–H_2O and $Zn(OTf)_2$–TEP–H_2O electrolytes. Reproduced with permission Adv. Funct. Mater. **31**, 2104281 (2021). Copyright 2021 Wiley.[67]

components to inorganic ZnF_2 while approaching the inner layer, to confirm the bilayer structure of SEI. This ionically conductive and electrically insulating SEI suppresses water decomposition and significant volume change of the inner part. Zn//MnO_2 battery with this electrolyte exhibited a high energy density of 168 W h kg^{-1} and capacity retention of 96.5% following 700 cycles at 10 C.[64] Zn-dendrite suppression ability (γE) of SEI compounds are compared. $Zn_3(PO_4)_2$ and ZnF_2 exhibits higher interfacial energy with Zn metal, for which Zn atoms preferentially move parallel to the interface layer instead of penetrating into the SEI [Fig. 15(e)]. Given the significant dendrite-suppression ability of $Zn_3(PO_4)_2$ and accelerated Zn^{2+} transport kinetics of ZnF_2, a $Zn_3(PO_4)_2$/ZnF_2-rich SEI results from unstable KPF_6 additive. The moisture-sensitive KPF_6 decomposes and takes part in the formation of the multi-functional interphase and optimizes cyclability of AZMBs.[68]

Except for these inorganic species, organic additives are found significant in regulating the electrolyte solvation structure or leading to protective SEI on zinc anode. In particular, sorbitol[91] and 2,3,4,5-tetrahydrothiophene-1,1-dioxide (TD)[92] lower the desolvation energy of the electrolyte and can dominantly adsorb on the zinc anode for rendering dendrite growth. In addition to salt decomposition derived SEI design strategy, a stable polydopamine (PDA) SEI can be obtained by *in situ* electrochemical polymerization of organic dopamine (DA) additive as illustrated in Fig. 15(f). The Zn anode cycled in electrolyte with addition of DA exhibits "smooth" morphology while a "rough" surface with obvious dendrite is generated in electrolyte without DA. The hydrophilic, adhesive PDA SEI leads to uniform Zn deposition, boosts Zn^{2+} transport kinetics and suppresses parasitic reactions.[70] These pioneering research has led to increased understanding of the import and practical use of additives in stabilizing Zn electrodes.

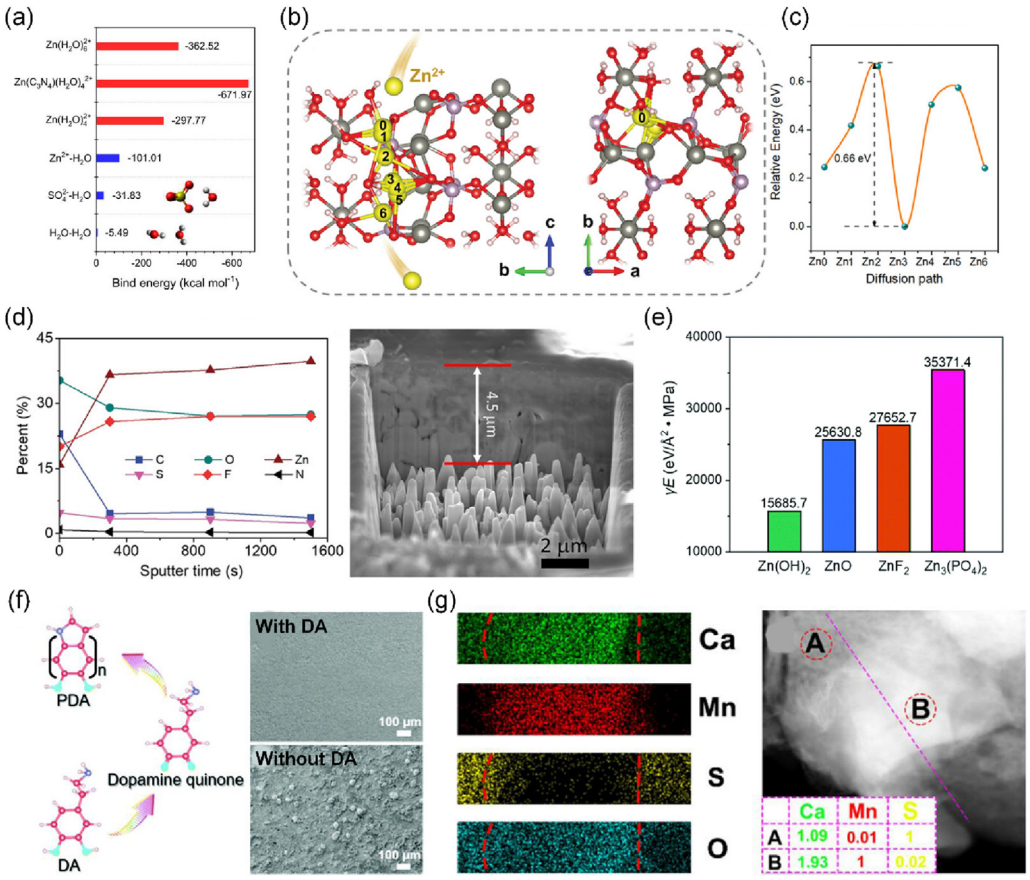

FIG. 15. Electrolyte additive strategy for AZMBs. (a) DFT computation for binding energy of Zn^{2+} solvation configurations. Reproduced with permission from Zhang *et al.*, Nat. Commun. **13**, 5348 (2022). Copyright 2022 Springer Nature.[71] (b) DFT computations for optimum Zn-ion diffusion pathway in SEI layer and (c) migration energy barrier. Reproduced with permission from Zeng *et al.*, Adv. Mater. **33**, e2007416 (2021). Copyright 2021 Wiley.[11] (d) Composition of SEI on Zn following 50 plating/stripping cycles in $Zn(OTf)_2$–$Zn(NO_3)_2$ electrolyte. Reproduced with permission from Li *et al.*, Angew. Chem., Int. Ed. Engl. **60**, 13035 (2021). Copyright 2021 Wiley.[64] (e) Capability of suppressing Zn dendrite (γE) for different SEI compounds. Reproduced with permission from Chu *et al.*, Energy Environ. Sci. **14**, 3609 (2021). Copyright 2021 The Royal Society of Chemistry.[68] (f) Illustration for PDA polymerization and SEM images of Zn electrodes cycled in electrolyte with/without DA. Reproduced with permission from Zeng *et al.*, Energy Environ. Sci. **14**, 5947 (2021). Copyright 2021 The Royal Society of Chemistry.[70] (g) Mapping image and elemental ratio analyses on film (A) and bulk (B). Reproduced with permission from Guo *et al.*, ACS Nano **13**, 13456 (2019). Copyright 2019 American Chemical Society.[93]

However, decisive conclusions cannot be drawn for cathode materials, especially inhibition of dissolution. Guo *et al.*[93] reported the generation of SEI layer composed of $CaSO_4{\cdot}2H_2O$ during electrochemically charging of Ca_2MnO_4 cathode for AZMBs. $CaSO_4{\cdot}2H_2O$ phase was confirmed from clear, core-shell mapping images of the cathode at the fully charged state. The Ca/Mn/S element ratios on film (A) and bulk (B) were 1.09:0.01:1 and 1.93:1:0.02, respectively, evidencing that the shell was $CaSO_4{\cdot}2H_2O$, and bulk was Ca_2MnO_4 in Fig. 15(g). *In situ* formed SEI layer on cathode obviated cathode dissolution, lowered impedance and reduced activation energy as ZMB operated for 1000 cycles without apparent capacity fade at a current density of 1 A g^{-1}.

4. Eutectic solvents

Deep eutectic solvents can practically regulate the coordination environment of multivalent metal electrolytes and are a novel strategy for designing multi-valent metal forms. The strong coordination of amides with cations and anions has enabled eutectic liquefaction of protic amide-based ligands with Zn salts containing Lewis basic anions, e.g., bis(trifluoromethylsulphonyl)imide ($TFSI^-$) following moderate heating.[94] Yang *et al.*[94] reported that an altered ionic coordination environment in acetamide-$Zn(TFSI)_2$ based eutectic electrolytes has a significant impact on the plating/stripping of Zn anodes and the appearance of a zinc fluoride-rich organic/inorganic hybrid SEI. DFT computations evidence that in the free $TFSI^-$ and the $TFSI^-$ complexed with Zn^{2+}, the redox potential for the former is lower than that for the Zn/Zn^{2+} pair, and the latter changes the reduction potential under interaction with Zn^{2+}. Findings confrimed that $TFSI^-$, which originally undergoes no reductive decomposition before Zn deposition, undergoes a more preferential reduction reaction than for Zn^{2+} following complexation with Zn^{2+}, as illustrated in Fig. 16(a). They confirmed also that $TFSI^-$ coordinates with Zn^{2+} and forms $[ZnTFSI_m(Ace)_n]^{(2-m)+}$ ($m = 1–2$ and $n = 1–3$) complex with

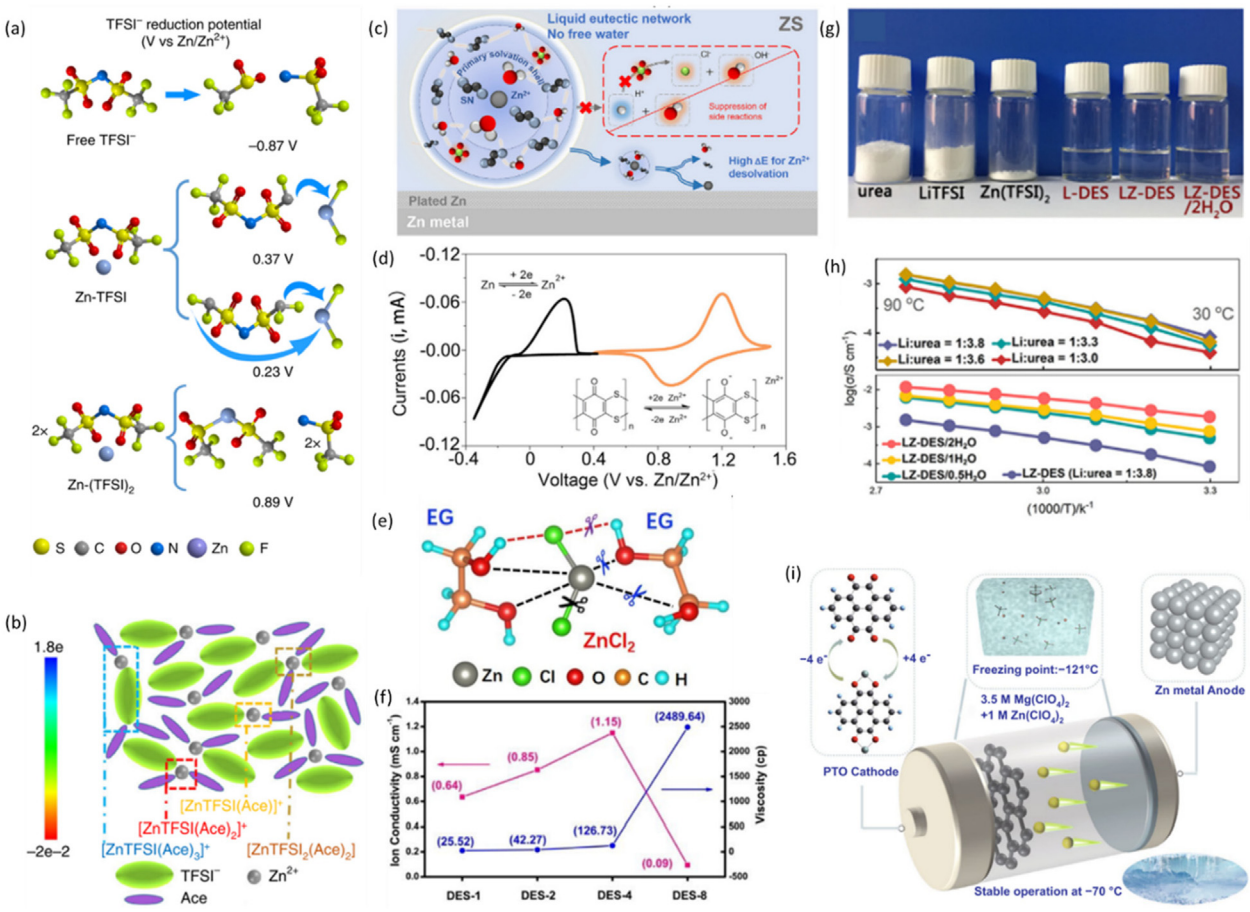

FIG. 16. Eutectic solvent strategy for AZMBs. (a) DFT computations for reduction potentials. (b) Scheme for $[ZnTFSI_2(Ace)_n]$ configuration. Reproduced with permission from Qiu *et al.*, Nat. Commun. **10**, 5374 (2019). Copyright 2019 Springer Nature.[72] (c) Scheme for Zn^{2+} solvation structure and interfacial reactions in ZS. (d) CV curves for Zn anode against PDB cathode in ZS. Reproduced with permission from Yang *et al.*, Joule **4**, 1557 (2020). Copyright 2020 Elsevier.[94] (e) Scheme for interaction between $ZnCl_2$ and EG. (f) Viscosity and ion conductivity for selected DES. Reproduced with permission from Geng *et al.*, Angew. Chem., Int. Ed. Engl. **61**, e202206717 (2022). Copyright 2022 Wiley.[73] (g) Stoichiometry for urea, LiTFSI and $Zn(TFSI)_2$ used to prepare L-DES, LZ-DES, and LZ-DES/$2H_2O$. (h) Ionic conductivity for LZ-DES and LZ-DES/nH_2O with varying water contents at different temperatures. Reproduced with permission from Zhao *et al.*, Nano Energy **57**, 625 (2019). Copyright 2019 Wiley.[95] (i) Scheme for Zn//PTO battery with 3.5 M $Mg(ClO_4)_2$ + 1 M $Zn(ClO_4)_2$ electrolyte. Reproduced with permission from Sun *et al.*, Nano-Micro Lett. **13**, 204 (2021). Copyright 2021 Springer Nature.[96]

multiple configurations in acetamide-$Zn(TFSI)_2$ eutectic electrolyte [Fig. 16(b)]. Later, to improve the ionic conductivity of the deep eutectic electrolyte, Qiu *et al.*[72] incorporated water molecules as chemical building blocks in eutectic networks via simply mixing hydrated Zn salt $[Zn(ClO_4)_2{\cdot}6H_2O]$ with a neutral ligand (succinonitrile, SN) in Fig. 16(c). Water molecules are reallocated in the eutectic electrolyte and $[Zn(OH_2)_x(SN)_y]^{2+}$ cations with regulated solvation structure boosts Zn reversibility and suppresses organic cathode dissolution to give stable cycling performance > 3500 cycles for Zn//poly(2,3-dithiino-1,4-benzoquinone) (PDB) battery [Fig. 16(d)]. Additionally, deep eutectic solvents obtained via heterogeneous cleavage of metal halides, e.g., $ZnCl_2$ with neutral ligands at low eutectic ratios have been extensively reported. A $ZnCl_2$/EG eutectic electrolyte has high conductivity of 1.15 mS cm^{-1} and a moderate viscosity of 126.73 cp when the molar ratio of $ZnCl_2$/EG is 4 (DES-4) [Fig. 16(f)]. The reduction of cations leads to the formation of Cl-rich SEI on the anode, giving reversible Zn stripping/plating of 3200 h. Zn//PANI based on DES-4 exhibited "superior" cycling with 78% capacity retention following 10 000 cycles.[73] A novel "water-in-DES" strategy is the addition of ~6 wt. % of water into urea/LiTFSI/$Zn(TFSI)_2$ DES [Fig. 16(g)]. Both eutectic features and advantages of the aqueous electrolyte, such as low viscosity (0.139 Pa s) and high ionic conductivity (1.85 mS cm^{-1}) for LZ-DES/$2H_2O$ at 30 °C, are maintained [Fig. 16(h)]. A Zn//$LiMn_2O_4$ battery based on LZ-DES/$2H_2O$ exhibited a "satisfactory" rechargeability with >90% capacity retention following 300 cycles.[95] Because of decreased H-bonds in water molecules by O-ligand Mg^{2+} and H-ligand ClO_4, 3.5 M $Mg(ClO_4)_2$ + 1 M $Zn(ClO_4)_2$ [Fig. 16(i)] exhibits a freezing point of −121 °C, a high ionic conductivity of 1.41 mS cm^{-1}, and a low viscosity of 22.9 mPa·s at −70 °C. The Zn//pyrene4,5,9,10-tetraone (PTO) battery delivered a discharge capacity of 101.5 mA h g^{-1} at −70 °C.[96]

TABLE III. Aqueous Mg^{2+} and Ca^{2+} ion batteries. (The symbol "*" represents there is no data available from the referred work.)

Battery	Electrolyte property				Full battery					Solid electrolyte interphase		
	Salt	Solvent(s)	ESW	Ionic conductivity (mS cm^{-1})	Cathode material	Anode material	Specific capacity (mAh g^{-1})	Current rate	Cycling number	CEI	SEI	Ref.
vs Mg/Mg^{2+}	1 m $MgSO_4$ 4 m $Mg(TFSI)_2$	H_2O	2.2–3.5 1.7–3.7	*	$Li_3V_2(PO_4)_3$	PPMDA	102	1 C	1000	*	*	99
	0.8 m $Mg(TFSI)_2$	85% PEG + 15% H_2O	0.48–4.18	0.183	V_2O_5	AC	286	50 mA g^{-1}	100	MgF_2	*	100
	$Mg(NO_3)_2$ $6H_2O$	Acetamide	*	*	CuHCF	PTCDA	45	10 C	2000	*	*	13
vs Ca/Ca^{2+}	8.37 m $Ca(NO_3)_2$	10 wt. % PVA + H_2O	1.86–4.46	11.56	$Ca_{0.4}MnO_2$	Sulfur/ carbon (S/C)	60	0.2 C	150	*	CaO, Ca_3N_2,Ca–S species (CaS, $Ca(HS)_2$), $CaCO_3$, $Ca(NO_3)_2$	104
	8.4 m $Ca(NO_3)_2$	H_2O	*	*	$CuFe(CN)_6$	*	65	10 C	5000	*	*	102

V. AQUEOUS MAGNESIUM- AND CALCIUM-ION BATTERIES

A. Electrolyte strategies for aqueous magnesium-ion batteries

The naturally formed MgO and $Mg(OH)_2$ film on Mg anode restricts practical application of aqueous Mg batteries. However, through electrolyte design, developments have been made, as shown in Table III.

An $MgCl_2$ WIS electrolyte was reported to minimize the water related side reaction and convert Mg^{2+} ion impermeable passivation film to the metallic oxide layer. Transformation of the passivation film into the Mg/MgO mixture was confirmed via the cross-sectional FIB-SEM image. The conversion with Cl^- is illustrated in Fig. 17(a). With reversible Mg dissolution and deposition, the Mg//CuHCF cell displays a high voltage plateau of 2.4–2.0 V, highly significant cycling performance of 700 cycles, and high CE of 99% at 0.5 A g^{-1}.[97] Another concentrated aqueous electrolyte using 4.5 m $Mg(NO_3)_2$ was reported to improve stability via preventing the PANI cathode from unalterable deprotonation. The content for four (4) types of N species in PANI charged and discharged in electrolytes of differing $Mg(NO_3)_2$ concentration is compared in Fig. 17(b). Protonated N (–NH^+– and –NH^+=) are maintained in 4.5 m $Mg(NO_3)_2$ during charge/discharge, giving a long lifespan for PANI with >10 000 cycles.[98] $Li_3V_2(PO_4)_3$ (LVP) and poly pyromellitic dianhydride (PPMDA) are reported to be excellent Mg ion host materials. Following delithiation of LVP in the first 10 cycles, reversible magnesiation/demagnesiation is established because of the high concentration of Mg^{2+} in the electrolyte [Fig. 17(c)]. Coupled with PPMDA of superior Na^+ and Li^+ intercalation ability, the AMIB with 4 m $Mg(TFSI)_2$ electrolyte exhibited a voltage of 1.9 V, high power density of 6400 W kg^{-1}, and good-capacity retention of 92% following 6000 cycles.[99]

However, practical application of WIS electrolyte is limited because of intrinsic disadvantages of high-cost and viscosity. Solvation structure for $Mg(TFSI)_2$ with low concentration is reorganized with the addition of PEG. To obviate these difficulties, an optimized 0.8 m $Mg(TFSI)_2$–85%PEG–15%H_2O electrolyte was used to exhibit an extended ESW of ~3.7 V [Fig. 17(d)].[100] A hydrated eutectic electrolyte design composed of acetamide and $Mg(NO_3)_2{\cdot}6H_2O$ was reported to prevent water induced performance degradation on organic electrodes, such as perylene-3,4,9,10-tetracarboxylic dianhydride (PTCDA), via tuning the hydrated structure of Mg^{2+}. Water content of electrolyte is carefully controlled by changing the n_{Mg2+}:$n_{acetamide}$ ratio [Fig. 17(e)]. As a result, a CuHCF//PTCDA full battery exhibits a high voltage of 2.2 V, an energy density of 52.2 W h kg^{-1}, and low temperature operation capability.[13] The insertion of Mg in birnessite phase MnO_2 was reported as a suitable cathode material in Fig. 17(f). The MnO_2 with Mg^{2+} in the nonaqueous system [0.25 M $Mg(TFSI)_2$ in diglyme] favors a conversion reaction with production of MnOOH, MnO, and $Mg(OH)_2$, while it changes to intercalation mechanism in an aqueous 0.5 M $Mg(ClO_4)_2$ electrolyte. Findings emphasized the significance of Mg^{2+} cation desolvation energy in nonaqueous systems.[101]

B. Electrolyte strategies for aqueous calcium-ion batteries

ACIBs are considered as alternatives to ALIBs because of high earth abundance and environmental friendliness of calcium. However,

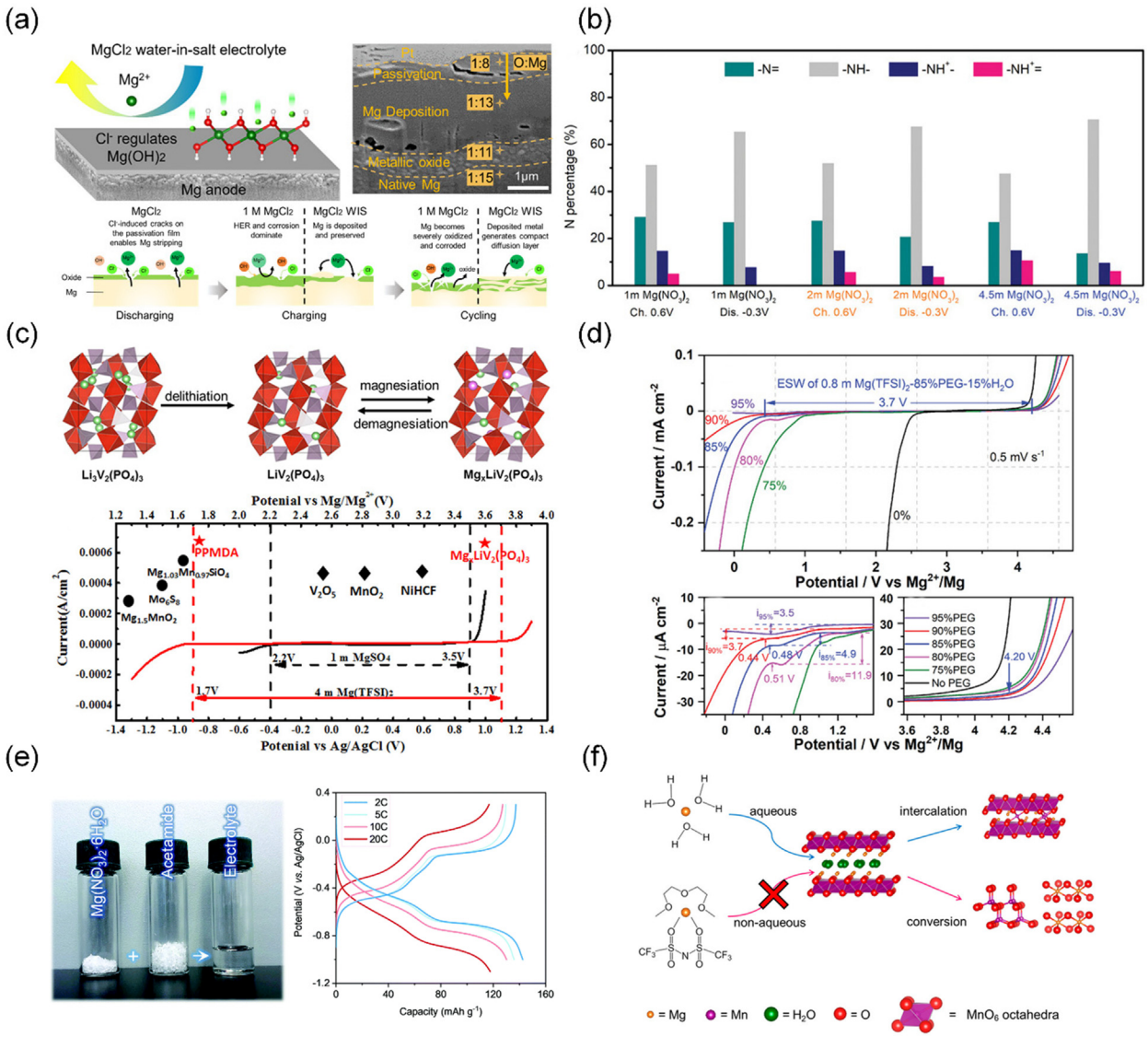

FIG. 17. Electrolyte strategy for AMIBs. (a) Suppressed side reaction and conversion from passivation film to metallic oxide complex via an $MgCl_2$ WIS electrolyte. Reproduced with permission from Leong *et al.*, ACS Energy Lett. **7**, 2657 (2022). Copyright 2022 American Chemical Society.[97] (b) Content of N species for PANI cathode at states indicated in selected electrolyte. Reproduced with permission from Zhu *et al.*, Adv. Funct. Mater. **31**, 2107523 (2021). Copyright 2021 Wiley.[98] (c) Scheme for working mechanism for the LVP cathode in 4 m $Mg(TFSI)_2$ electrolyte. Reproduced with permission from Wang *et al.*, ACS Cent. Sci. **3**, 1121 (2017). Copyright 2017 American Chemical Society.[99] (d) ESWs for 0.8 m $Mg(TFSI)_2$-xPEG-$(1-x)H_2O$ (x = 0%, 75%, 80%, 85%, 90%, and 95%). Reproduced with permission from Fu *et al.*, Adv. Funct. Mater. **32**, 2110674 (2022). Copyright 2022 Wiley.[100] (e) Hydrated eutectic electrolyte with n_{Mg2+}: $n_{acetamide}$ = 1:8 and charge–discharge curves. Reproduced with permission from Zhu *et al.*, Energy Environ. Sci. **15**, 1282 (2022). Copyright 2022 The Royal Society of Chemistry.[13] (f) Scheme for working mechanism for MnO_2 in MIB with nonaqueous/aqueous electrolyte. Reproduced with permission from Sun *et al.*, Chem. Mater. **28**, 534 (2016). Copyright 2016 American Chemical Society.[101]

narrow ESW for dilute aqueous electrolyte and large radius for hydrated Ca^{2+} ions induced instability of host materials during (de)intercalating hinders practical application of ACIBs. WIS is a practical strategy to decrease the hydration number of Ca^{2+} ions to give lower radius of hydrated Ca^{2+} ions and activation energy of Ca^{2+} ion insertion. The smooth insertion/extraction significantly boosts electrochemical performance of the system in terms of the discharge/charge capacities, rate capability, and cyclability.[102] The $Ca(NO_3)_2$ salt is preferred for WIS electrolyte because of its high solubility of 20 m at 25 °C and low-cost. A 20 m $Ca(NO_3)_2$ WIS electrolytes exhibited a window expansion of ∼0.96 V compared with that for diluted 1 m electrolyte [Fig. 18(a)].[103] Exploiting the synergistic effect between concentrated $Ca(NO_3)_2$ and aqueous polyvinyl alcohol (PVA) gel, ESW for as-prepared aqueous gel electrolyte was expanded to 2.6 V and enveloped the electrochemical redox couple of sulfur anode and $Ca_{0.4}MnO_2$ cathode [Fig. 18(b)]. The $Ca_{0.4}MnO_2$//sulfur full cell

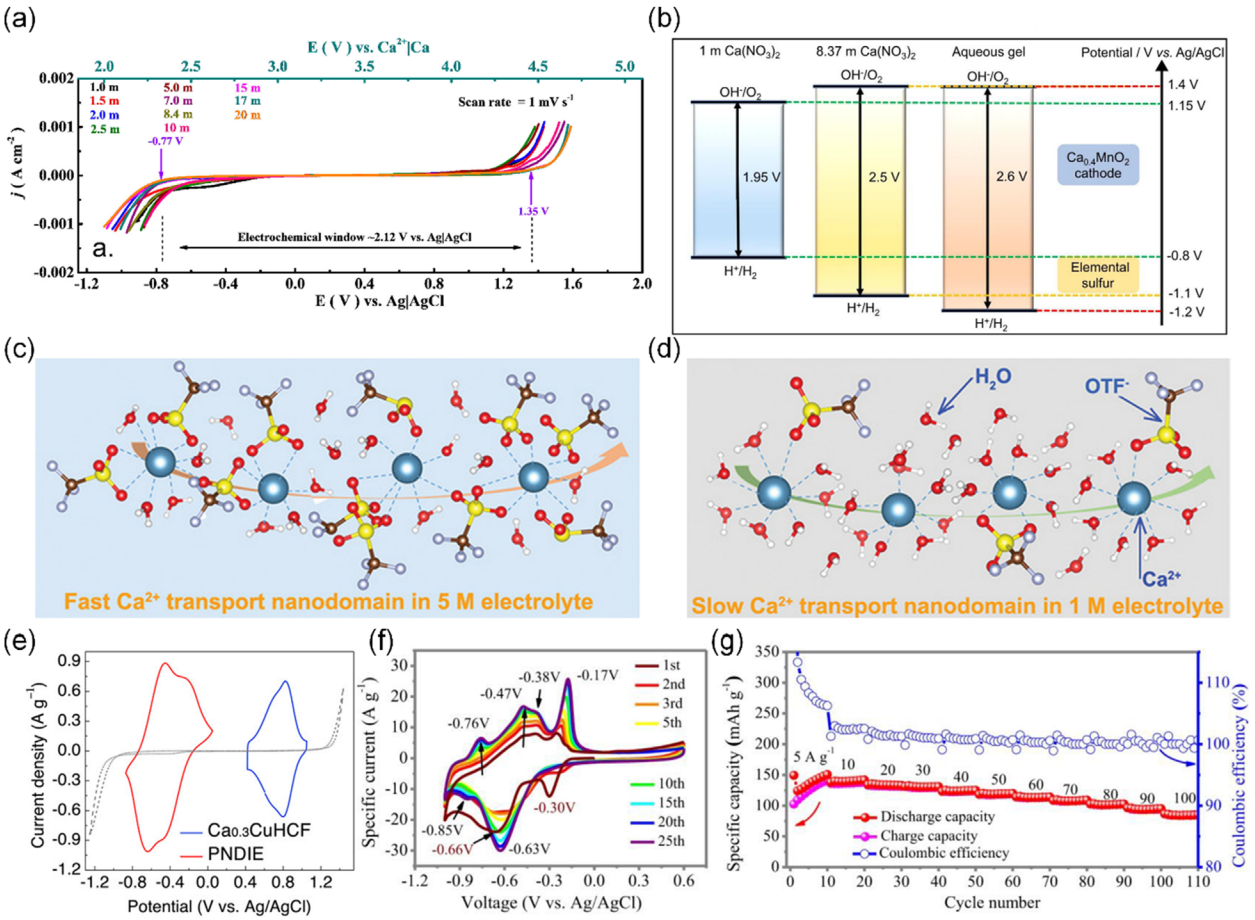

FIG. 18. Electrolyte strategy for ACIBs. (a) ESWs for $Ca(NO_3)_2$ aqueous electrolyte of varying concentration. Reproduced with permission from Adil *et al.*, ACS Appl. Mater. Interfaces **14**, 25501 (2022). Copyright 2022 American Chemical Society.[103] (b) ESWs of 1 m, 8.37 m $Ca(NO_3)_2$ and aqueous gel, electrolyte, and redox voltages for the $Ca_{0.4}MnO_2$ cathode and sulfur anode. Reproduced with permission from Nat. Commun. **12**, 2857 (2021). Copyright 2021 Springer Nature.[104] Schematic for transport nanochannels for hydrated Ca-ions in (c) 5 and (d) 1 M electrolytes. Reproduced with permission from Tong *et al.*, Adv. Funct. Mater. **31**, 2104639 (2021). Copyright 2021 Wiley.[105] (e) CV curves for $Ca_{0.3}$CuHCF and PNDIE in 2.5 m $Ca(NO_3)_2$ and electrochemical stability of electrolyte. Reproduced with permission from Gheytani *et al.*, Adv. Sci. (Weinheim, Ger.) **4**, 1700465 (2017). Copyright 2017 Wiley.[14] (f) CV curves for PT anode in 1 M $CaCl_2$ solution and (g) specific capacity for PT in 1 M $CaCl_2$ at selected current density and corresponding Coulombic efficiency (CE). Reproduced with permission from Han *et al.*, Nat. Commun. **12**, 2400 (2021). Copyright 2021 Springer Nature.[106]

exhibited excellent cyclability and a specific energy of 110 W h kg^{-1}.[104] Concentration of electrolytes affect transport process of Ca^{2+} ion. The high concentration electrolyte using 5 M $Ca(OTf)_2$ [Fig. 18(c)] was found with lower ion diffusion activation energy and much faster transport kinetics than that using 1 M $Ca(OTf)_2$ [Fig. 18(d)]. Hydrated Ca^{2+} ions in 5 M $Ca(OTf)_2$ move rapidly because of electrostatic interaction with the consecutive electronegative OTf^- channels while Ca^{2+} ions in 1 M $Ca(OTf)_2$ exhibited sluggish diffusion as they are isolated by a significant H_2O molecules.[105]

Development of cathode and anode materials for reversible storage of Ca^{2+} is necessary to establish rapid and stable CIB. Polyimide poly[N,N′-(ethane-1,2-diyl)-1,4,5,8-naphthalenetetracarboxiimide] (PNDIE) and CuHCF were selected as anode and cathode because the redox potentials are located within ESW of 2.5 m $Ca(NO_3)_2$ electrolyte [Fig. 18(e)]. With the combination of PNDIE anode with high capacity and rate capability and CuHCF with low structure-strain accommodating Ca^{2+}, the full cell exhibited excellent cycling performance at both low and high current density.[14] 5,7,12,14-pentacenetetrone (PT) molecules construct internal channels via weak π–π stacked layers and, the robust structure accommodates Ca^{2+} ions and accelerates ion diffusion. Following activation of PT within initial several cycles, the full battery exhibited a highly significant specific capacity of 150.5 mA h g^{-1} at 5 A g^{-1}, good capacity retention, and the ability to operate at high current density of 100 A g^{-1} [106] and, therefore, is practically attractive [Figs. 18(g) and 18(h)].

VI. CONCLUSION AND OUTLOOK

A. Summary and comparison

The present five (5) design strategies for liquid aqueous electrolyte have differing advantages, performance, and potential for practical application [Fig. 19(a)]. The hybrid solvent and additive design

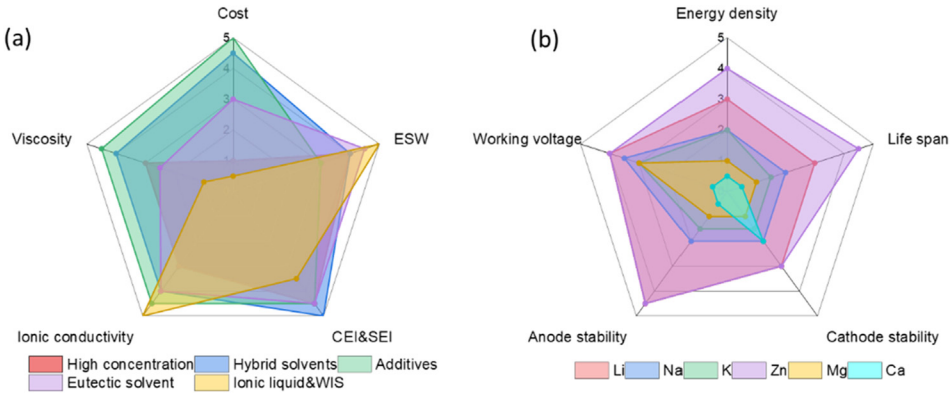

FIG. 19. Spider chart for (a) five (5) electrolyte strategies (high concentration, hybrid solvents, additives, eutectic solvent, and ionic liquid–WIS) over low electrolyte cost, competitive physical properties (viscosity and ionic conductivity), protective CEI&SEI formation ability and wide ESW; and (b) six (6) M-ion (M = Li, Na, K, Zn, Mg, and Ca) battery chemistries over high energy density, high working voltage, good anode and cathode stability, and long life span.

strategies are the best for electrolyte cost and low-viscosity, while the high concentration and ionic liquid–WIS strategies are not presently ideal.

An increased ESW can be achieved with strategies that include ionic liquid–WIS, eutectic solvents, high concentration, and hybrid solvents, given that free water molecules can be reduced and that water decomposition can be suppressed through ions or solvent interactions with water. Unlike reduced ionic conductivity when adding certain solvent or eutectic components, a superhigh ionic conductivity can be practically synthesized in ionic liquid–WIS, while the additive and hybrid solvent designs maintain relatively high ionic transportation ability of the aqueous electrolyte. CEI and SEI are more likely to be synthesized via hybrid solvents, eutectic solvents, and high concentration pathways, because this offer oxidation or reduction species for interphases formation(s).

Importantly, the current six (6) ARBs chemistries are unbalanced [Fig. 19(b)], because of different choices for electrode and electrolyte materials. The original physical property of the metal ions results in different desolvation kinetics. Significant research has focused on ALIBs and AZMBs that are practically promising because of relative, high-energy density. ALIBs exhibit > 100 W h kg^{-1} under a eutectic electrolyte, while AZMBs, 160 W h kg^{-1}. Compared with unwanted, significant dendrites with Zn metal, the anode for ALIBs represented by LTO is significantly more stable. The cycling life for the full ALIBs is not as competitive as with AZMBs, possibly because of cathode instability. A representative cathode material LMO usually exhibits the drawback of Mn dissolution and irreversible phase transformation to MnO_2 following the first charge cycle, resulting in a fast-fading capacity. Similar dissolution occurs with AZMBs, as many high-capacity cathode active materials, such as vanadium oxides, react slowly with water following structural collapse. Inferior stability of cathode and anode under aqueous electrolyte requires a sustained effort in building protective electrode/electrolyte interphases, together with improved understanding of electrolyte structure and decomposing mechanism(s).

To conclude, regarding challenges in the discussed six aqueous batteries chemistries, the high concentration and hybrid and eutectic solvents are practically promising for developing high energy density ARBs. To improve the cycling life of ARBs, future research is needed to focus on boosting ESW for the electrolyte and increasing the understanding of the electrode/electrolyte interface stability via new CEI/SEI compositions and structures.

B. Outlook on electrolyte and electrode/electrolyte interphase study

Given the significance of electrolyte design in determining energy density, electrode stability, and fast charge/discharge, future development of ARBs for high power output and good cyclability will need a systematic study and be dependent on electrolytes and electrode/electrolyte interfaces, which requires both advanced characterizations and computational methods.

Spectroscopies, including Raman and FT-IR, and NMR are conventional tools for developing primary insight into electrolyte solvation structure. However, these are not sufficient to provide necessary in-depth data and avoid superficial answers for design and behavior of electrolytes over coordination environments around cations because of peak overlap and restricted accuracy for low naturally abundance elements. Quantitative understanding of the electrode/electrolyte interphase needs reliable *in situ* techniques, including *in situ* Raman, FT-IR, and pH monitoring, to observe dynamic change on electrode surfaces in real-time charge/discharge. Advanced study of both static and dynamic electrolyte and interface is needed to develop quantitative electrolyte design principles.

Simulation will be a useful method to aid increasing understanding of electrolyte behavior, because properly used, it reduces the need to practically test all. Figure 20 presents a summary outlook for electrode–electrolyte modeling strategies for advanced electrolyte and interphase design in aqueous batteries. A correlation between solvation structure (short-range ordering structure), free water molecules, and interfacial parasitic reactions, including self-corrosion and H_2 evolution, has been established and will need confirmation and development. Information on reduction potential for different complexes will be assessed with DFT to guide formation of protective CEI and SEI film on the electrode surface, while at the same time, inhibiting detrimental water decomposition reaction and aiding quantitative determination of the origin of self-corrosion and H_2 evolution. Critical electrolyte physical properties, including ionic conductivity and viscosity, will be able to be simulated reliably to predict long-range ordering behavior, therefore improving electrolyte selection.

In future, based on these accurate and reliable MD simulations, WIS will be more widely used to control ESW and formation of protective interphase on the surface. Direct investigation of electrode/electrolyte interface will be made possible to understand changes in electrochemical activity, e.g., adsorption, charge-transfer, interphase

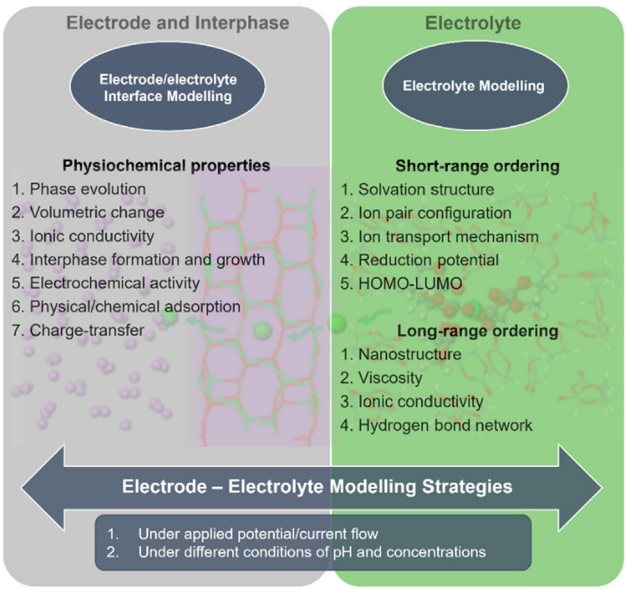

FIG. 20. Left: Predicted physicochemical properties of electrode/electrolyte interface from modeling strategies for accelerating the design of advanced electrolyte interphase; right: short-range and long-range ordering behaviors of electrolytes that could be analyzed by electrolyte modeling.

formation, and ion-transport/storage mechanisms, e.g., ionic conductivity, phase evolution, and volumetric change, in either the absence or presence of interphase. Increasing computational modeling power and methods for solid/liquid interface and liquid systems are expected to facilitate *in silico* design of electrode and electrolyte.

This review overall will be of benefit in the design of water-based electrolyte(s) for stable electrode materials and interfaces, and therefore, achieving high-performance and long cycling life aqueous batteries.

SUPPLEMENTARY MATERIAL

See the supplementary material for Fig. S1.

ACKNOWLEDGMENTS

This work was supported by the Australian Research Council Discovery Projects (Nos. DP200101862 and FL210100050) and the Australian Institute of Nuclear Science and Engineering-Early Career Research Grant.

AUTHOR DECLARATIONS

Conflict of Interest

The authors have no conflicts to disclose.

Author Contributions

Sailin Liu: Conceptualization (lead); Writing – original draft (lead); Writing – review & editing (lead). **Ruizhi Zhang:** Writing – original draft (supporting); Writing – review & editing (equal). **Jianfeng Mao:** Writing – review & editing (equal). **Jodie A. Yuwono:** Writing – original draft (supporting); Writing – review & editing (supporting). **Cheng Wang:** Writing – review & editing (supporting). **Kenneth Richard Davey:** Writing – review & editing (equal). **Zaiping Guo:** Supervision (lead); Writing – original draft (equal); Writing – review & editing (lead).

DATA AVAILABILITY

Data sharing is not applicable to this article as no new data were created or analyzed in this study.

REFERENCES

[1]D. Wu, X. Li, X. Liu, J. Yi, P. Acevedo-Peña, E. Reguera, K. Zhu, D. Bin, N. Melzack, R. G. A. Wills, J. Huang, X. Wang, X. Lin, D. Yu, and J. Ma, J. Phys. Energy **4**(4), 041501 (2022).
[2]S. Liu, R. Zhang, J. Mao, Y. Zhao, Q. Cai, and Z. Guo, Sci. Adv. **8**, eabn5097 (2022).
[3]F. Zhang, W. Zhang, D. Wexler, and Z. Guo, Adv. Mater. **34**(24), e2107965 (2022).
[4]J. Xu and C. Wang, J. Electrochem. Soc. **169**(3), 030530 (2022).
[5]L. S. Suo, O. B. Borodin, T. Gao, M. Olguin, J. Ho, X. Fan, C. Luo, C. Wang, and K. Xu, Science **350**(6263), 938 (2015).
[6]J. Xu, X. Ji, J. Zhang, C. Yang, P. Wang, S. Liu, K. Ludwig, F. Chen, P. Kofinas, and C. Wang, Nat. Energy **7**(2), 186–193 (2022).
[7]D. Chao, W. Zhou, F. X. Xie, C. Ye, H. Li, M. Jaroniec, and S.-Z. Qiao, Sci. Adv. **6**(21), eaba4098 (2020).
[8]K. Nakamoto, R. Sakamoto, Y. Nishimura, J. Xia, M. Ito, and S. Okada, Electrochemistry **89**(5), 415–419 (2021).
[9]S. Ko, Y. Yamada, and A. Yamada, Electrochem. Commun. **116**, 106764 (2020).
[10]Z. Zhao, R. Wang, C. Peng, W. Chen, T. Wu, B. Hu, W. Weng, Y. Yao, J. Zeng, Z. Chen, P. Liu, Y. Liu, G. Li, J. Guo, H. Lu, and Z. Guo, Nat. Commun. **12**(1), 6606 (2021).
[11]X. Zeng, J. Mao, J. Hao, J. Liu, S. Liu, Z. Wang, Y. Wang, S. Zhang, T. Zheng, J. Liu, P. Rao, and Z. Guo, Adv. Mater. **33**(11), e2007416 (2021).
[12]M. Li, Y. Ding, Y. Sun, Y. Ren, J. Yang, B. Yin, H. Li, S. Zhang, and T. Ma, Mater. Rep.: Energy **2**, 100161 (2022).
[13]Y. Zhu, X. Guo, Y. Lei, W. Wang, A.-H. Emwas, Y. Yuan, Y. He, and H. N. Alshareef, Energy Environ. Sci. **15**(3), 1282–1292 (2022).
[14]S. Gheytani, Y. Liang, F. Wu, Y. Jing, H. Dong, K. K. Rao, X. Chi, F. Fang, and Y. Yao, Adv. Sci. (Weinheim, Ger.) **4**(12), 1700465 (2017).
[15]S. Dühnen, J. Betz, M. Kolek, R. Schmuch, M. Winter, and T. Placke, Small Methods **4**(7), 2000039 (2020).
[16]A. Wang, S. Kadam, H. Li, S. Shi, and Y. Qi, npj Comput. Mater. **4**(1), 15 (2018).
[17]Y. Shang, N. Chen, Y. Li, S. Chen, J. Lai, Y. Huang, W. Qu, F. Wu, and R. Chen, Adv. Mater. **32**(40), e2004017 (2020).
[18]L. Suo, O. Borodin, W. Sun, X. Fan, C. Yang, F. Wang, T. Gao, Z. Ma, M. Schroeder, A. von Cresce, S. M. Russell, M. Armand, A. Angell, K. Xu, and C. Wang, Angew. Chem., Int. Ed. Engl. **55**(25), 7136–7141 (2016).
[19]C. Lee, Y. Yokoyama, Y. Kondo, Y. Miyahara, T. Abe, and K. Miyazaki, Adv. Energy Mater. **11**(25), 2100756 (2021).
[20]S. Liu, D. Liu, S. Wang, X. Cai, K. Qian, F. Kang, and B. Li, J. Mater. Chem. A **7**(21), 12993–12996 (2019).
[21]F. Wang, Y. Lin, L. Suo, X. Fan, T. Gao, C. Yang, F. Han, Y. Qi, K. Xu, and C. Wang, Energy Environ. Sci. **9**(12), 3666–3673 (2016).
[22]J. Chen, J. Vatamanu, L. Xing, O. Borodin, H. Chen, X. Guan, X. Liu, K. Xu, and W. Li, Adv. Energy Mater. **10**(3), 1902654 (2019).
[23]P. Jaumaux, X. Yang, B. Zhang, J. Safaei, X. Tang, D. Zhou, C. Wang, and G. Wang, Angew. Chem., Int. Ed. Engl. **60**(36), 19965–19973 (2021).
[24]X. Hou, T. P. Pollard, W. Zhao, X. He, X. Ju, J. Wang, L. Du, E. Paillard, H. Lin, K. Xu, O. Borodin, M. Winter, and J. Li, Small **18**(5), e2104986 (2022).
[25]Z. Ma, J. Chen, J. Vatamanu, O. Borodin, D. Bedrov, X. Zhou, W. Zhang, W. Li, K. Xu, and L. Xing, Energy Storage Mater. **45**, 903–910 (2022).

[26]Y. Wang, T. Wang, D. Dong, J. Xie, Y. Guan, Y. Huang, J. Fan, and Y.-C. Lu, Matter **5**(1), 162–179 (2022).
[27]X. Zhang, J. Chen, Z. Xu, Q. Dong, H. Ao, Z. Hou, and Y. Qian, Energy Storage Mater. **46**, 147–154 (2022).
[28]S. Ko, Y. Yamada, and A. Yamada, ACS Appl. Mater. Interfaces **11**(49), 45554–45560 (2019).
[29]L. Chen, J. Zhang, Q. Li, J. Vatamanu, X. Ji, T. P. Pollard, C. Cui, S. Hou, J. Chen, C. Yang, L. Ma, M. S. Ding, M. Garaga, S. Greenbaum, H.-S. Lee, O. Borodin, K. Xu, and C. Wang, ACS Energy Lett. **5**(3), 968–974 (2020).
[30]C. Zhang, B. Chen, Z. Cai, F. Zhang, R. Huang, M. Yan, Y. Liu, and H. Pan, J. Mater. Chem. A **10**(38), 20545–20551 (2022).
[31]J. Y. Luo, W. J. Cui, P. He, and Y. Y. Xia, Nat. Chem. **2**(9), 760–765 (2010).
[32]T. Mendez-Morales, Z. Li, and M. Salanne, Batteries Supercaps **4**(4), 646–652 (2020).
[33]W. Sun, L. Suo, F. Wang, N. Eidson, C. Yang, F. Han, Z. Ma, T. Gao, M. Zhu, and C. Wang, Electrochem. Commun. **82**, 71–74 (2017).
[34]C. Yang, J. Chen, T. Qing, X. Fan, W. Sun, A. von Cresce, M. S. Ding, O. Borodin, J. Vatamanu, M. A. Schroeder, N. Eidson, C. Wang, and K. Xu, Joule **1**(1), 122–132 (2017).
[35]J. Zheng, G. Tan, P. Shan, T. Liu, J. Hu, Y. Feng, L. Yang, M. Zhang, Z. Chen, Y. Lin, J. Lu, J. C. Neuefeind, Y. Ren, K. Amine, L.-W. Wang, K. Xu, and F. Pan, Chem **4**(12), 2872–2882 (2018).
[36]C. Yang, L. Suo, O. Borodin, F. Wang, W. Sun, T. Gao, X. Fan, S. Hou, Z. Ma, K. Amine, K. Xu, and C. Wang, Proc. Natl. Acad. Sci. U. S. A. **114**(24), 6197–6202 (2017).
[37]W. Deng, X. Wang, C. Liu, C. Li, J. Chen, N. Zhu, R. Li, and M. Xue, Energy Storage Mater. **20**, 373–379 (2019).
[38]F. Wang, O. Borodin, M. S. Ding, M. Gobet, J. Vatamanu, X. Fan, T. Gao, N. Eidson, Y. Liang, W. Sun, S. Greenbaum, K. Xu, and C. Wang, Joule **2**(5), 927–937 (2018).
[39]J. Xie, Z. Liang, and Y. C. Lu, Nat. Mater. **19**(9), 1006–1011 (2020).
[40]R. Lin, C. Ke, J. Chen, S. Liu, and J. Wang, Joule **6**(2), 399–417 (2022).
[41]B. B. Hansen, S. Spittle, B. Chen, D. Poe, Y. Zhang, J. M. Klein, A. Horton, L. Adhikari, T. Zelovich, B. W. Doherty, B. Gurkan, E. J. Maginn, A. Ragauskas, M. Dadmun, T. A. Zawodzinski, G. A. Baker, M. E. Tuckerman, R. F. Savinell, and J. R. Sangoro, Chem. Rev. **121**(3), 1232–1285 (2021).
[42]P. Jiang, L. Chen, H. Shao, S. Huang, Q. Wang, Y. Su, X. Yan, X. Liang, J. Zhang, J. Feng, and Z. Liu, ACS Energy Lett. **4**(6), 1419–1426 (2019).
[43]Z. Hou, M. Dong, Y. Xiong, X. Zhang, Y. Zhu, and Y. Qian, Adv. Energy Mater. **10**(15), 1903665 (2020).
[44]M. Becker, D. Rentsch, D. Reber, A. Aribia, C. Battaglia, and R. S. Kuhnel, Angew. Chem., Int. Ed. Engl. **60**(25), 14100–14108 (2021).
[45]H. S. Dhattarwal and H. K. Kashyap, J. Phys. Chem. B **126**(28), 5291–5304 (2022).
[46]H. Zhang, X. Liu, H. Li, I. Hasa, and S. Passerini, Angew. Chem., Int. Ed. Engl. **60**(2), 598–616 (2021).
[47]L. Suo, O. Borodin, Y. Wang, X. Rong, W. Sun, X. Fan, S. Xu, M. A. Schroeder, A. V. Cresce, F. Wang, C. Yang, Y. S. Hu, K. Xu, and C. Wang, Adv. Energy Mater. **7**(21), 1701189 (2017).
[48]T. Jin, X. Ji, P. F. Wang, K. Zhu, J. Zhang, L. Cao, L. Chen, C. Cui, T. Deng, S. Liu, N. Piao, Y. Liu, C. Shen, K. Xie, L. Jiao, and C. Wang, Angew. Chem., Int. Ed. Engl. **60**(21), 11943–11948 (2021).
[49]J. Han, H. Zhang, A. Varzi, and S. Passerini, ChemSusChem **11**(21), 3704–3707 (2018).
[50]R.-S. Kühnel, D. Reber, and C. Battaglia, ACS Energy Lett. **2**(9), 2005–2006 (2017).
[51]H. Zhang, S. Jeong, B. Qin, D. Vieira Carvalho, D. Buchholz, and S. Passerini, ChemSusChem **11**(8), 1382–1389 (2018).
[52]M. H. Lee, S. J. Kim, D. Chang, J. Kim, S. Moon, K. Oh, K.-Y. Park, W. M. Seong, H. Park, G. Kwon, B. Lee, and K. Kang, Mater. Today **29**, 26–36 (2019).
[53]H. Bi, X. Wang, H. Liu, Y. He, W. Wang, W. Deng, X. Ma, Y. Wang, W. Rao, Y. Chai, H. Ma, R. Li, J. Chen, Y. Wang, and M. Xue, Adv. Mater. **32**(16), e2000074 (2020).
[54]H. Zhang, B. Qin, J. Han, and S. Passerini, ACS Energy Lett. **3**(7), 1769–1770 (2018).
[55]P. Jiang, Z. Lei, L. Chen, X. Shao, X. Liang, J. Zhang, Y. Wang, J. Zhang, Z. Liu, and J. Feng, ACS Appl. Mater. Interfaces **11**(32), 28762–28768 (2019).
[56]Q. Nian, J. Wang, S. Liu, T. Sun, S. Zheng, Y. Zhang, Z. Tao, and J. Chen, Angew. Chem., Int. Ed. Engl. **58**(47), 16994–16999 (2019).
[57]H. Ao, C. Chen, Z. Hou, W. Cai, M. Liu, Y. Jin, X. Zhang, Y. Zhu, and Y. Qian, J. Mater. Chem. A **8**(28), 14190–14197 (2020).
[58]Q. Nian, X. Zhang, Y. Feng, S. Liu, T. Sun, S. Zheng, X. Ren, Z. Tao, D. Zhang, and J. Chen, ACS Energy Lett. **6**(6), 2174–2180 (2021).
[59]L. Jiang, Y. Lu, C. Zhao, L. Liu, J. Zhang, Q. Zhang, X. Shen, J. Zhao, X. Yu, H. Li, X. Huang, L. Chen, and Y.-S. Hu, Nat. Energy **4**(6), 495–503 (2019).
[60]T. Liu, L. Tang, H. Luo, S. Cheng, and M. Liu, Chem. Commun. (Cambridge, U. K.) **55**(85), 12817–12820 (2019).
[61]J. Han, A. Mariani, H. Zhang, M. Zarrabeitia, X. Gao, D. V. Carvalho, A. Varzi, and S. Passerini, Energy Storage Mater. **30**, 196–205 (2020).
[62]Y. Li, W. Deng, Z. Zhou, C. Li, M. Zhang, X. Yuan, J. Hu, H. Chen, and R. Li, J. Mater. Chem. A **9**(5), 2822–2829 (2021).
[63]F. Ming, Y. Zhu, G. Huang, A. H. Emwas, H. Liang, Y. Cui, and H. N. Alshareef, J. Am. Chem. Soc. **144**(16), 7160–7170 (2022).
[64]D. Li, L. Cao, T. Deng, S. Liu, and C. Wang, Angew. Chem., Int. Ed. Engl. **60**(23), 13035–13041 (2021).
[65]S. Liu, J. P. Vongsvivut, Y. Wang, R. Zhang, F. Yang, S. Zhang, K. Davey, J. Mao, and Z. Guo, Angew. Chem. **135**(4), e202215600 (2023).
[66]L. Cao, D. Li, E. Hu, J. Xu, T. Deng, L. Ma, Y. Wang, X. Q. Yang, and C. Wang, J. Am. Chem. Soc. **142**(51), 21404–21409 (2020).
[67]S. Liu, J. Mao, W. K. Pang, J. Vongsvivut, X. Zeng, L. Thomsen, Y. Wang, J. Liu, D. Li, and Z. Guo, Adv. Funct. Mater. **31**(38), 2104281 (2021).
[68]Y. Chu, S. Zhang, S. Wu, Z. Hu, G. Cui, and J. Luo, Energy Environ. Sci. **14**(6), 3609–3620 (2021).
[69]L. Cao, D. Li, T. Pollard, T. Deng, B. Zhang, C. Yang, L. Chen, J. Vatamanu, E. Hu, M. J. Hourwitz, L. Ma, M. Ding, Q. Li, S. Hou, K. Gaskell, J. T. Fourkas, X. Q. Yang, K. Xu, O. Borodin, and C. Wang, Nat. Nanotechnol. **16**(8), 902–910 (2021).
[70]X. Zeng, K. Xie, S. Liu, S. Zhang, J. Hao, J. Liu, W. K. Pang, J. Liu, P. Rao, Q. Wang, J. Mao, and Z. Guo, Energy Environ. Sci. **14**(11), 5947–5957 (2021).
[71]W. Zhang, M. Dong, K. Jiang, D. Yang, X. Tan, S. Zhai, R. Feng, N. Chen, G. King, H. Zhang, H. Zeng, H. Li, M. Antonietti, and Z. Li, Nat. Commun. **13**(1), 5348 (2022).
[72]H. Qiu, X. Du, J. Zhao, Y. Wang, J. Ju, Z. Chen, Z. Hu, D. Yan, X. Zhou, and G. Cui, Nat. Commun. **10**(1), 5374 (2019).
[73]L. Geng, J. Meng, X. Wang, C. Han, K. Han, Z. Xiao, M. Huang, P. Xu, L. Zhang, L. Zhou, and L. Mai, Angew. Chem., Int. Ed. Engl. **61**(31), e202206717 (2022).
[74]L. Ma, M. A. Schroeder, O. Borodin, T. P. Pollard, M. S. Ding, C. Wang, and K. Xu, Nat. Energy **5**(10), 743–749 (2020).
[75]D. Kundu, B. D. Adams, V. Duffort, S. H. Vajargah, and L. F. Nazar, Nat. Energy **1**(10), 16119 (2016).
[76]Y. Wang, Z. Wang, F. Yang, S. Liu, S. Zhang, J. Mao, and Z. Guo, Small **18**(43), e2107033 (2022).
[77]Q. Zhang, K. Xia, Y. Ma, Y. Lu, L. Li, J. Liang, S. Chou, and J. Chen, ACS Energy Lett. **6**(8), 2704–2712 (2021).
[78]G. Yang, J. Huang, X. Wan, B. Liu, Y. Zhu, J. Wang, O. Fontaine, S. Luo, P. Hiralal, Y. Guo, and H. Zhou, EcoMat **4**(2), e12165 (2022).
[79]N. Patil, C. Cruz, D. Ciurduc, A. Mavrandonakis, J. Palma, and R. Marcilla, Adv. Energy Mater. **11**(26), 2100939 (2021).
[80]F. Yang, J. A. Yuwono, J. Hao, J. Long, L. Yuan, Y. Wang, S. Liu, Y. Fan, S. Zhao, K. Davey, and Z. Guo, Adv. Mater. **34**(45), e2206754 (2022).
[81]F. Wang, O. Borodin, T. Gao, X. Fan, W. Sun, F. Han, A. Faraone, J. A. Dura, K. Xu, and C. Wang, Nat. Mater. **17**(6), 543–549 (2018).
[82]C. Zhang, J. Holoubek, X. Wu, A. Daniyar, L. Zhu, C. Chen, D. P. Leonard, I. A. Rodriguez-Perez, J. X. Jiang, C. Fang, and X. Ji, Chem. Commun. (Cambridge, U. K.) **54**(100), 14097–14099 (2018).
[83]T. Sun, X. Yuan, K. Wang, S. Zheng, J. Shi, Q. Zhang, W. Cai, J. Liang, and Z. Tao, J. Mater. Chem. A **9**(11), 7042–7047 (2021).
[84]S. Cai, X. Chu, C. Liu, H. Lai, H. Chen, Y. Jiang, F. Guo, Z. Xu, C. Wang, and C. Gao, Adv. Mater. **33**(13), e2007470 (2021).
[85]Y. S. Meng, V. Srinivasan, and K. Xu, Science **378**(6624), eabq3750 (2022).
[86]N. Chang, T. Li, R. Li, S. Wang, Y. Yin, H. Zhang, and X. Li, Energy Environ. Sci. **13**(10), 3527–3535 (2020).

[87]H. Du, K. Wang, T. Sun, J. Shi, X. Zhou, W. Cai, and Z. Tao, Chem. Eng. J. **427**, 131705 (2022).
[88]J. Hao, L. Yuan, C. Ye, D. Chao, K. Davey, Z. Guo, and S. Z. Qiao, Angew. Chem., Int. Ed. Engl. **60**(13), 7366–7375 (2021).
[89]Z. Rong, R. Malik, P. Canepa, G. Sai Gautam, M. Liu, A. Jain, K. Persson, and G. Ceder, Chem. Mater. **27**(17), 6016–6021 (2015).
[90]V. V. Kulish and S. Manzhos, RSC Adv. **7**(30), 18643–18649 (2017).
[91]Y. Quan, M. Yang, M. Chen, W. Zhou, X. Han, J. Chen, B. Liu, S. Shi, and P. Zhang, Chem. Eng. J. **458**, 141392 (2023).
[92]K. Wang, T. Qiu, L. Lin, X.-X. Liu, and X. Sun, Energy Storage Mater. **54**, 366–373 (2023).
[93]S. Guo, S. Liang, B. Zhang, G. Fang, D. Ma, and J. Zhou, ACS Nano **13**(11), 13456–13464 (2019).
[94]W. Yang, X. Du, J. Zhao, Z. Chen, J. Li, J. Xie, Y. Zhang, Z. Cui, Q. Kong, Z. Zhao, C. Wang, Q. Zhang, and G. Cui, Joule **4**(7), 1557–1574 (2020).
[95]J. Zhao, J. Zhang, W. Yang, B. Chen, Z. Zhao, H. Qiu, S. Dong, X. Zhou, G. Cui, and L. Chen, Nano Energy **57**, 625–634 (2019).
[96]T. Sun, S. Zheng, H. Du, and Z. Tao, Nano-Micro Lett. **13**(1), 204 (2021).
[97]K. W. Leong, W. Pan, Y. Wang, S. Luo, X. Zhao, and D. Y. C. Leung, ACS Energy Lett. **7**(8), 2657–2666 (2022).
[98]Y. Zhu, J. Yin, A. H. Emwas, O. F. Mohammed, and H. N. Alshareef, Adv. Funct. Mater. **31**(50), 2107523 (2021).
[99]F. Wang, X. Fan, T. Gao, W. Sun, Z. Ma, C. Yang, F. Han, K. Xu, and C. Wang, ACS Cent. Sci. **3**(10), 1121–1128 (2017).
[100]Q. Fu, X. Wu, X. Luo, S. Indris, A. Sarapulova, M. Bauer, Z. Wang, M. Knapp, H. Ehrenberg, Y. Wei, and S. Dsoke, Adv. Funct. Mater. **32**(16), 2110674 (2022).
[101]X. Sun, V. Duffort, B. L. Mehdi, N. D. Browning, and L. F. Nazar, Chem. Mater. **28**(2), 534–542 (2016).
[102]C. Lee and S.-K. Jeong, Electrochim. Acta **265**, 430–436 (2018).
[103]M. Adil, A. Ghosh, and S. Mitra, ACS Appl. Mater. Interfaces **14**(22), 25501–25515 (2022).
[104]X. Tang, D. Zhou, B. Zhang, S. Wang, P. Li, H. Liu, X. Guo, P. Jaumaux, X. Gao, Y. Fu, C. Wang, C. Wang, and G. Wang, Nat. Commun. **12**(1), 2857 (2021).
[105]Z. Tong, T. Kang, Y. Wan, R. Yang, Y. Wu, D. Shen, S. Liu, Y. Tang, and C. S. Lee, Adv. Funct. Mater. **31**(41), 2104639 (2021).
[106]C. Han, H. Li, Y. Li, J. Zhu, and C. Zhi, Nat. Commun. **12**(1), 2400 (2021).
[107]C. Yang, J. Chen, X. Ji, T. P. Pollard, X. Lü, C.-J. Sun, S. Hou, Q. Liu, C. Liu, T. Qing, Y. Wang, O. Borodin, Y. Ren, K. Xu, and C. Wang, Nature **569**(7755), 245–250 (2019).
[108]D. Sun, M. Okubo, and A. Yamada, Chem. Sci. **12**(12), 4450–4454 (2021).
[109]S. Kondou, E. Nozaki, S. Terada, M. L. Thomas, K. Ueno, Y. Umebayashi, K. Dokko, and M. Watanabe, J. Phys. Chem. C **122**(35), 20167–20175 (2018).
[110]D. Liu, Q. Yu, S. Liu, K. Qian, S. Wang, W. Sun, X.-Q. Yang, F. Kang, and B. Li, J. Phys. Chem. C **123**(20), 12797–12806 (2019).
[111]J. M. Wrogemann, S. Künne, A. Heckmann, I. A. Rodríguez-Pérez, V. Siozios, B. Yan, J. Li, M. Winter, K. Beltrop, and T. Placke, Adv. Energy Mater. **10**(8), 1902709 (2020).
[112]Q. Dou, Y. Wang, A. Wang, M. Ye, R. Hou, Y. Lu, L. Su, S. Shi, H. Zhang, and X. Yan, Sci. Bull. **65**(21), 1812–1822 (2020).
[113]X. Zhan and M. Shirpour, Chem. Commun. **53**(1), 204–207 (2017).
[114]K. Nakamoto, R. Sakamoto, M. Ito, A. Kitajou, and S. Okada, Electrochemistry **85**(4), 179–185 (2017).
[115]Y. Yokoyama, T. Fukutsuka, K. Miyazaki, and T. Abe, J. Electrochem. Soc. **165**(14), A3299–A3303 (2018).
[116]D. Reber, R.-S. Kühnel, and C. Battaglia, ACS Mater. Lett. **1**(1), 44–51 (2019).
[117]R. Sakamoto, M. Yamashita, K. Nakamoto, Y. Zhou, N. Yoshimoto, K. Fujii, T. Yamaguchi, A. Kitajou, and S. Okada, Phys. Chem. Chem. Phys. **22**(45), 26452–26458 (2020).
[118]Q. Zheng, S. Miura, K. Miyazaki, S. Ko, E. Watanabe, M. Okoshi, C.-P. Chou, Y. Nishimura, H. Nakai, T. Kamiya, T. Honda, J. Akikusa, Y. Yamada, and A. Yamada, Angew. Chem., Int. Ed. Engl. **58**(40), 14202–14207 (2019).
[119]D. Reber, R. Grissa, M. Becker, R.-S. Kühnel, and C. Battaglia, Adv. Energy Mater. **11**(5), 2002913 (2021).
[120]D. Su, A. McDonagh, S.-Z. Qiao, and G. Wang, Adv. Mater. **29**(1), 1604007 (2017).
[121]Y. Li, Z. Zhou, W. Deng, C. Li, X. Yuan, J. Hu, M. Zhang, H. Chen, and R. Li, ChemElectroChem **8**(8), 1451–1454 (2021).
[122]B. W. Olbasa, F. W. Fenta, S.-F. Chiu, M.-C. Tsai, C.-J. Huang, B. A. Jote, T. T. Beyene, Y.-F. Liao, C.-H. Wang, W.-N. Su, H. Dai, and B. J. Hwang, ACS Appl. Energy Mater. **3**(5), 4499–4508 (2020).
[123]J. Hao, L. Yuan, Y. Zhu, M. Jaroniec, and S. Z. Qiao, Adv. Mater. **34**(44), e2206963 (2022).